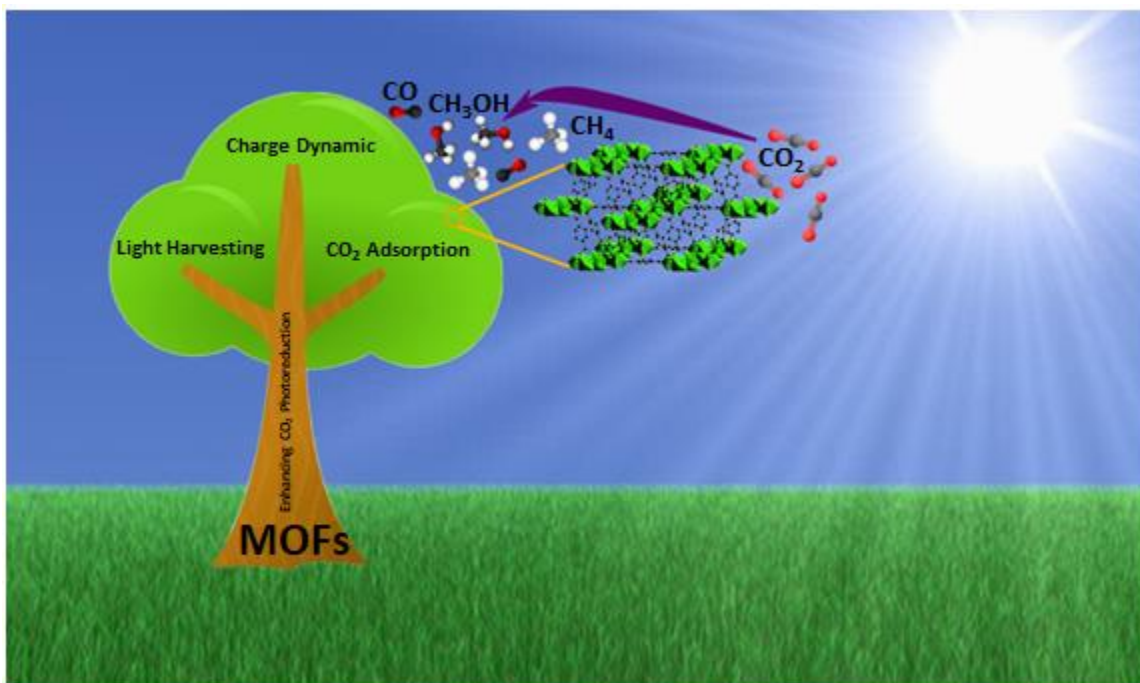


## Engineering metal-organic frameworks for efficient photocatalytic conversion of CO<sub>2</sub> into solar fuels

Submitted version made available in agreement with publisher's policy

Please, cite as follows:

Chizoba I. Ezugwu, Shengwei Liu, Chuanhao Li, Serge Zhuiykov, Soumyajit Roy, Francis Verpoort, Engineering metal-organic frameworks for efficient photocatalytic conversion of CO<sub>2</sub> into solar fuels, Coordination Chemistry Reviews 450 (2022) 214245, <https://doi.org/10.1016/j.ccr.2021.214245>



## Engineering metal-organic frameworks for efficient photocatalytic conversion of CO<sub>2</sub> into solar fuels

Chizoba I. Ezugwu<sup>a,b</sup>, Shengwei Liu<sup>\*a</sup>, Chuanhao Li<sup>a</sup>, Serge Zhuiykov<sup>d</sup>, Soumyajit Roy<sup>e\*</sup>, Francis Verpoort<sup>\*c,d</sup>

<sup>a</sup>School of Environmental Science and Engineering, Guangdong Provincial Key Laboratory of Environmental Pollution Control and Remediation Technology, Sun Yat-sen University, Guangzhou 510006, P. R. China.

<sup>b</sup>Department of Analytical Chemistry, Physical Chemistry and Chemical Engineering, University of Alcalá, Alcalá de Henares, E-28871 Madrid, Spain

<sup>c</sup>State Key Laboratory of Advanced Technology for Materials Synthesis and Processing, Wuhan University of Technology, Wuhan 430070, P. R. China

<sup>d</sup>Center for Environmental & Energy Research, Ghent University Global Campus, Incheon 21985, South Korea.

<sup>e</sup>Department of Chemical Sciences, Indian Institute of Science Education and Research, Kolkata, Mohanpur 741246, India.

\*Corresponding authors: liushw6@mail.sysu.edu.cn (S. Liu), roy.soumyajit@googlemail.com (S. Roy), francis.verpoort@ghent.ac.kr (F. Verpoort)

### Abstract

Artificial photosynthesis is an emerging and reliable technique for CO<sub>2</sub> mitigation, and it is also a potential method to achieve carbon dioxide resourcing and efficiently convert solar energy to storable high-density chemical energy (solar fuels), solving both the challenging universal problems of energy shortage and global warming simultaneously. Metal-organic frameworks (MOFs) are crystalline materials composed of metal ions bridged by organic ligands to form one to three-dimensional coordination networks. MOFs are emerging photocatalysts with the highest surface area compared to other photocatalytic materials known to humankind, and their flexible rational design allows the incorporation of different active sites into a particular framework, thereby generating a complex multicomponent photocatalytic system. This review surveys the updated strategies to rationally design a photocatalytic MOFs for efficient transformation of CO<sub>2</sub> into solar fuels. The review discusses MOFs' features as semiconductor photocatalysts, and diverse means of improving their light-harvesting, charge separation and CO<sub>2</sub> adsorption capacity. Furthermore, different components of MOFs that are light-responsive and the light-harvesting mechanisms for the CO<sub>2</sub> photoreduction are highlighted. The breath of work compiled in this review will stimulate further research in global CO<sub>2</sub> abatement and will be of great importance to broad ranges of researchers and industrialists.

**Keywords:** Metal-organic frameworks, Photocatalysis, Artificial photosynthesis, Solar fuels, Carbon dioxide reduction

## Contents

1. Introduction
2. MOFs as semiconductor photocatalysts
  - 2.1. Conductivity of MOFs
  - 2.2. Potentials, advantages and challenges of MOFs for photocatalysis
  - 2.3. Mechanism of CO<sub>2</sub> reduction and selectivity of the product
3. Engineering the light-harvesting components of MOF
  - 3.1. Functionalization of organic ligands
  - 3.2. Bandgap engineering
  - 3.3. Introducing metal complexes as bridging ligand
  - 3.4. Activation of metal nodes
  - 3.5. Mechanism of light-harvesting and electron transfer
4. Improving the charge dynamics of MOF photocatalysts
  - 4.1. Plasmonic Enhancement by Metal loading
  - 4.2. MOFs based composite photocatalysts
  - 4.3. Double metal node by doping
5. Enhancing the CO<sub>2</sub> adsorption of MOF photocatalysts
  - 5.1. Organic-linker modification
  - 5.2. Metal-nodes engineering
  - 5.3. Morphology Control
6. Conclusions and future perspectives

## 1. Introduction

In the atmospheric system, an increased amount of CO<sub>2</sub> results in a high imbalance in the influx of energy in the earth, thereby leading to a rise in the global temperature [1, 2]. Consequences to this increment are the melting of the ice caps and transformation of cultivatable land to desert, which might result in the rise in sea level, and the loss of hospitable space and climate of human habitat, in the near future [3]. Depletion of natural resources

and the resultant generation of waste gases mainly emanate from the scale of human activities. Notwithstanding that our daily energy needs still strongly depend on fossil fuels because of their stability, availability, and high energy density, it causes greenhouse gas emissions, hence threatening the current human living condition [3-6]. Hitherto, CO<sub>2</sub> evolved from the burning of hydrocarbon fuel like coal, natural gas, and oil is the worst climate pollutant standing at the forefront

of anthropogenic greenhouse gases [7, 8]. Notably, the environment is not only being polluted, but there is a continuing decline in oil supplies, thus humans are losing essential resources for modern civilization [1]. Utilizing sunlight as a source of alternative clean energy to efficiently transform CO<sub>2</sub> into important solar fuels could solve both of these challenging universal problems of energy shortage and global warming simultaneously [9-11]. Eons ago, green plants used a network of membrane-bounded chromophores to harvest solar energy that photochemically transforms carbon dioxide and water into energy-rich carbohydrates by natural photosynthesis [12-15]. Notwithstanding the abundant radiation of sunlight to our planet, an infinitesimal portion is utilized (the earth receives more solar energy per hour than is consumed per year); humanity needs to harness even less than 0.002% of available solar energy in order to accomplish our entire energy requirement [16, 17].

The development of solar fuels is of optimum importance since they are concentrated energy carriers, possess long-term energy storage capacity, and are environmentally benign [18, 19]. Solar fuels are predicted to become a vital contributor to humankind's energy needs in the near future and are also useful in balancing our yearly and daily variation in solar irradiation [20]. Thus, photosynthesis remains the biological blueprint for solar energy storage as fuels [21-23]. Solar fuels can be produced from sunlight by an indirect pathway with intermediate energy carriers such as the conversion of biomass to biogas or by a direct pathway, which involves an integrated system like

artificial photosynthesis [18]. The most promising solar fuels generated from artificial photosynthesis are carbon-based fuels that are produced by CO<sub>2</sub> reduction [24, 25]. Unlike hydrogen generated fuels, carbon-based fuels have proven to possess very dense energy storage [26, 27]. However, a robust practical solar-driven catalyst for carbon-based fuel production has not yet been discovered.

One of the foremost important environmental and climate issues is devising strategies and materials to reduce the concentration of CO<sub>2</sub> in the environment [4]. To avoid or delay the CO<sub>2</sub> emission into the atmosphere; carbon fixation has been achieved by both natural and artificial techniques such as photosynthesis, forestation, mineral carbonation, ocean fertilization, sequestration, direct ocean dump and geological injection [28, 29]. But some of these methods just store the CO<sub>2</sub> in its original form [30]. Furthermore, both means of removing the CO<sub>2</sub> from the flue exhaust (chilling and pressurizing the exhaust or passing through a fluidized bed of amine) are both inefficient and costly. Artificial photosynthesis is an emerging and reliable technique for CO<sub>2</sub> abatement. It is also a potential method to achieve carbon dioxide resourcing and efficiently convert energy from the sun to storable high-density chemical energy [31-33]. Consequently, researchers have employed both organic and inorganic materials to construct artificial photochemical systems [34]. Artificial photosynthesis was first reported in 1972, by using TiO<sub>2</sub> for water splitting [35]. Tremendous efforts have been geared toward producing other efficient

heterogeneous photocatalysts that include both semiconducting materials,  $\text{TiO}_2$ ,  $\text{CdS}$ ,  $\text{ZnO}$ ,  $\text{Zn}_2\text{GeO}_4$ , and  $\text{ZnGa}_2\text{O}_4$ , together with metal incorporated zeolites for  $\text{CO}_2$  reduction [11, 36-43]. But the performances of most of these materials are quite low because of low surface area, insufficient  $\text{CO}_2$  adsorption capacity, inferior light absorption efficiency, and low recorded charge separation efficiency. Thus, novel advanced photocatalyst systems and their modification strategies are still highly desirable.

The emerging of metal-organic framework (MOFs) as promising efficient, cost-effective, visible-light responsive materials with tunable and large gas adsorption capacity is believed to have high potentials of solving the long time environmental  $\text{CO}_2$  emission problems [44, 45]. MOFs are crystalline materials composed of metal ions [46] coordinated to organic linking groups (ligands) to form well oriented coordination networks [47-49]. Their frameworks contain abundant voids [50, 51]. Until now, MOFs have demonstrated the highest surface areas and the lowest densities compared to other materials known to humanity [52, 53]. Owing to the inherent enormous internal surface areas, high porosity, good chemical stability and varying topology of MOFs, they have emerged as outstanding hybrid material with numerous applications ranging from gas adsorption/separation/sequestration [54, 55], drug delivery [56, 57], chemical sensing [58, 59], dye adsorption/degradation [60, 61] and catalysis [62-67]. Moreover, those remarkable physicochemical properties of MOFs are adjustable

by rational selection and combination of metal nodes, organic linkers, and solvent together with the synthetic conditions [68]. The idea for the synthesis of these materials is achieved from metal carboxylate cluster chemistry. Hence, MOFs are recent development between material sciences and coordination chemistry [69]. Significantly, MOFs can be employed as semiconductor photocatalysts since they can absorb solar light to generate charge carriers which will then be transported to the targeted reactants and activate them to trigger photocatalytic redox reactions [70]. During these processes, they function as light-energy transducers to energize the charge carriers. Some studies have reported the use of MOFs as photocatalyst for diverse applications, including photocatalytic  $\text{CO}_2$  conversion [71-76]. The main challenge of achieving an efficient photosynthetic system is integrating the three functional modules for artificial photosynthesis [77], that is, light absorption center, charge transport pathway, and adsorption and reaction active sites, cooperatively in the single photocatalyst material system [78]. Different functional components, like photosensitizers [79] and catalytic site, can be flexibly integrated into a porous cavity of MOFs by host-guest synergetic design, making it of great potential to efficiently promote the three fundamental steps of photosynthesis in a hybrid MOFs based photocatalyst system [14]. Therefore, MOFs have the possibility to achieve artificial photosynthesis [80-82].

This review provides a comprehensive overview of the available strategies of tuning

metal-organic frameworks for enhanced photocatalytic CO<sub>2</sub> conversion into solar fuels. First, the inherent characteristics of MOFs as semiconductor photocatalysts are discussed. Subsequently, the light absorptive components of MOFs and the reaction mechanisms for CO<sub>2</sub> transformation are further highlighted. Then, the diverse approaches to enhance the charge dynamics performance of MOFs for photocatalytic CO<sub>2</sub> reduction are elaborated. Afterward, the available means for improving the CO<sub>2</sub> adsorption capacity of MOF photocatalysts are introduced. Finally, the challenges and further developments of MOF photocatalyst for CO<sub>2</sub> conversion into solar fuels are envisioned.

## 2. MOFs as semiconductor photocatalysts

Basically, semiconductors are inorganic photocatalysts, which the electron (e<sup>-</sup>) can be excited and migrate to the conduction band upon light radiation [83]. Due to the mobility of the excited e<sup>-</sup> in the conduction band, charge separation occurs and a positive vacant hole (h<sup>+</sup>) is left behind the valence band, as shown in Fig. 1a [84, 85]. This is the basic hallmark of a semiconductor. The electron will be transferred from the surface of the semiconductor to the substrate to initiate the reaction. The fundamental of photocatalytic processes lies in the optimized combination of charge separation and interfacial electron transfer [86, 87]. A function of the balance between these two processes, together with the energy-wasting charge recombination, determines the effectiveness of a photocatalyst [84, 88, 89].

In the inorganic aluminosilicate frameworks, zeolites are widely applied as catalysts in the petrochemical industries for their thermal and chemical robustness coupled with the ease in which the acid site can be formed [90]. But the potentials of zeolites as advanced functional materials are limited because of the inertness of the aluminosilicate structure and the difficulty in exciting the material by solar light [91, 92]. Zeolites are photochemically inert; hence they behave as insulators, and tuning zeolite to obtain a framework of desired application is difficult [93]. Although MOFs were regarded as poor conductors because of the small p-orbital conjugation of the organic ligand, the work of Allendorf using MOFs in microelectronic devices instigated scientists to integrate electrical conductivity within the framework materials [94]. They are functional hybrid materials, whose easy structural tunability and multifunctionality make them more versatile than inorganic or organic semiconductors [94, 95]. Kobayashi et al. [96] reported the first convincing semiconductive (p-type) porous Cu-based MOFs with an optical bandgap of 2 eV. The redox-active metal nodes in the MOFs provide charge mobility through the framework and their conductivity is temperature-dependent. Cu[Ni(pdt)<sub>2</sub>] was further doped by using I<sub>2</sub> as an oxidant, and the resultant porous framework has an enhanced conductivity by four orders of magnitude [96]. Not only as a p-type semiconductor but also the MOF frameworks can perform as an n-type semiconductor [94, 95].

The metal nodes of MOFs can be considered as discrete inorganic semiconductor entities

connected to the organic ligand, which are regarded as antennas that absorb light to activate these quantum dots [97, 98]. In this regard, these materials display photocatalytic features that are like that of conventional semiconductors. In particular, their photo-induced ligand-to-metal charge transfer (LMCT) together with the  $\pi-\pi^*$  excitation of the ligand, are observed at the ultraviolet and the blue end of visible regions, characteristic of similar band gap values to conventional semiconductors [14]. Zecchina and co-worker [99] first demonstrated the quantum dot behavior of metal clusters in MOF-5 by testifying that the metal node ( $\text{Zn}_4\text{O}_{13}$ ) behaves like a ZnO quantum dot (QD). The ZnO's absorption edge appears at 380 nm (near UV region); thus, ZnO was categorized as a wide band gap semiconductor. Since O(2p) and Zn(4s) orbitals are the major contributors to the valence and the conduction band of ZnO, respectively, it was deduced that this electronic transition in MOF-5 could be described as  $\text{O}^{2-}\text{Zn}^{2+} \rightarrow \text{O}^-\text{Zn}^+$  LMCT mechanism. The UV-Vis spectra of this material (Fig. 1b, solid curve) has a peak centered at 290 nm and an absorption edge at 350 nm, attributed to the ligand and the inorganic  $\text{Zn}_4\text{O}_{13}$  centers, respectively [99]. The SBU of the MOFs is represented in Fig. 1c. The edge at 350 nm experienced a blue shift of  $2300\text{ cm}^{-1}$  as compared to that of ZnO, because of the confinement effects. The  $\text{O}^{2-}\text{Zn}^{2+} \rightarrow \text{O}^-\text{Zn}^+$  transition confirms that the ZnO in the node acts as quantum dot [99]. In contrast, pure zeolites cannot absorb radiations of wavelengths longer than 220 nm. The semiconductor behavior of MOFs

was supported by Garcia and co-workers [93], which reported that upon light absorption based on the LMCT mechanism, the framework undergoes charge separation generating electrons and holes. By using laser Flash photolysis, it was detected that delocalized electrons live in microseconds to the CB in order to reduce viologen to viologen radicals. On the other hand, the  $\text{h}^+$  on the VB of the MOF oxidized N,N,N,N-tetramethyl-phenylenediamine.

Just like the CB and VB in a typical semiconductor, the HOMO and LUMO in MOFs play the same role [100]. Thus, upon photoexcitation of the framework, electrons migrate from the HOMO to the LUMO, resulting in charge separation. For example, the semiconductivity of Mn-MOFs was attributed to the delocalization and excitation of the  $\pi$ -electron from the HOMO to the LUMO [101]. The photogenerated electrons can be transferred from the LUMO to initiate reduction process and the  $\text{h}^+$  in the HOMO can oxidize a substrate. Unfortunately, electron-hole recombination can occur. In general, the organic ligand is the main contributor to the HOMO and the LUMO is mainly from the metal cluster [102, 103]. Theoretically, the energy for the MOF's HOMO-LUMO level is usually calculated by DFT calculation. The combination of the organic and inorganic components, coupled with the unique properties of MOFs, make them potential next generation semiconductive material for the electronic industries.

Along with the LMCT mechanism,  $\pi$ - $\pi$  interaction of ligands-induced semiconductor behavior is also proposed for some MOFs [104, 105]. It has been reported that manganese-based MOFs with pyrazine bridge exhibited semiconducting property [106]. The electron transfer mechanism through compact columnar aromatic  $\pi$ - $\pi$  interaction in the framework was used to explain the electrical conductivity, Fig. 1d. The HOMO-LUMO gaps were decreased by the  $\pi$ - $\pi$  interaction.

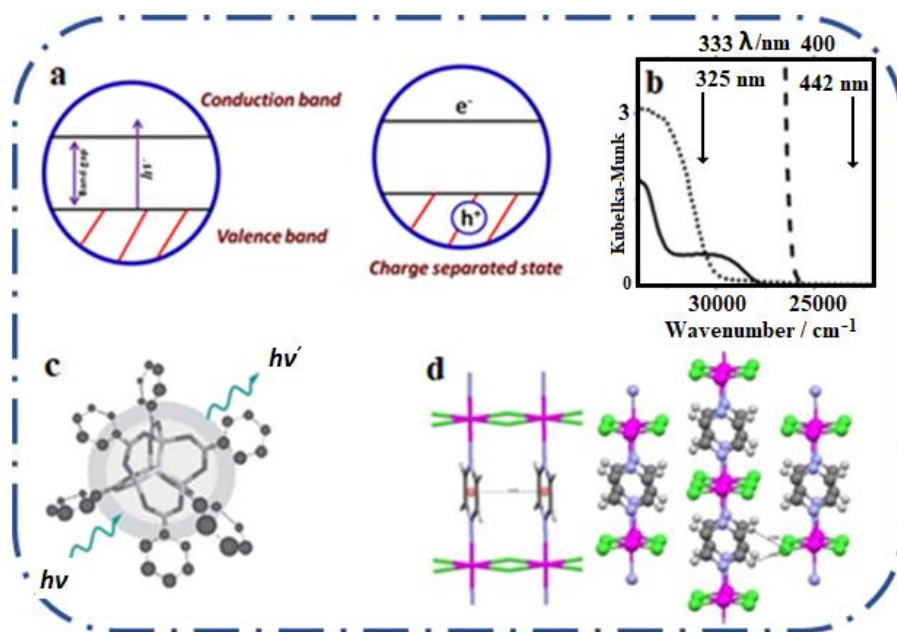
## 2.1. Conductivity of MOFs

The two main charge transport mechanisms in MOFs are hopping transport and band transport; both requiring low-energy pathway, thus higher orbital overlap improves charge mobility [107, 108]. Hopping transport occurs in a thermally

activated framework when a localized charge carrier at a particular site with discrete energy jump between neighboring sites.

Clough et al. reported a highly charge mobility framework, 2D Cobalt 2,3,6,7,10,11-triphenylenehexathiolate, which experienced a transition from semiconducting (between 300 and 170 K) to a metallic phase (at temperatures below 130 K) with decrease in temperature [109].

The high electrical conductivity was due to the efficient overlap between the metal node frontier orbitals and the linker. However, band transport involves delocalized electrons [110], and it occurs in materials with strong covalent bonding, which allows the formation of continuous energy bands [111]. Band transport is more versatile strategy in MOFs, thus more efforts have been geared toward



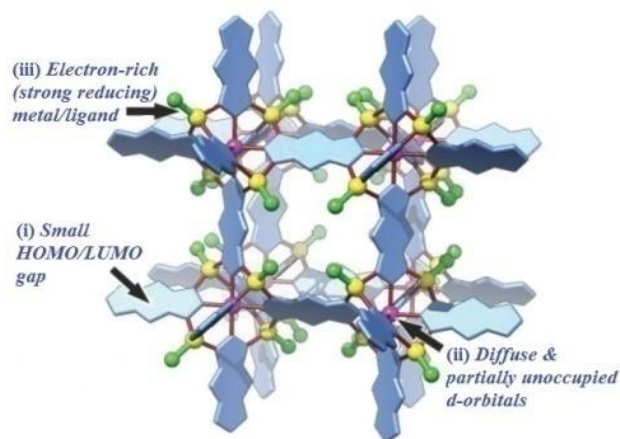
**Fig. 1** (a) Excitation of an electron to generate charge separated state. (b) UV-Vis spectra (c) the  $Zn_4O_{13}$  cluster of MOF-5. Reproduced with permission [96]. Copyright 2004, The Royal Society of Chemistry. (d)  $\pi$ - $\pi$  interaction between two pyrazine rings and  $CH\cdots Cl$  interaction between the adjacent layers. Reproduced with permission [97]. Copyright 2012, Elsevier.



building highly conductive MOFs by engineering the band transport regime [112]. The charge transport within the framework can be improved by  $\pi$ - $\pi$  stacking and mixed valency, which in turn increase the magnitude of charge delocalization. Murase et al. showed that mixed-valence can cause higher charge delocalization and conductivity in MOFs and semiconducting graphene-based materials [113].

By experimental measurements and theoretical calculations, a 3D Strontium-based MOF with an organic ligand 1,3,5-benzenetricarboxylic acid, exhibited remarkable semiconducting behavior (band gap 2.3 eV) and electrical conductivity of  $10^{-6}$  (S cm $^{-1}$ ) [114]. The value of this band gap is comparable to traditional semiconducting materials like CdTe, GaP, CdSe, and others [115, 116]. It was observed that Sr-based MOF has semiconducting transport behavior since the conductivity obeys the Arrhenius plot [114]. Volkmer and co-workers [117] reported three systematic trends of engineering the band gaps of semiconductor MOFs (Fig. 2). Firstly, by tuning the degree of the conjugation of the ligand, they illustrated that increased conjugation leads to higher valence band (HOMO) energy, thus resulting in a reduced band gap (HOMO-LUMO gap). Secondly, band gaps of MOFs are reduced by choosing an appropriate metal, like the Co $^{2+}$  in Co-MFU-4, whose diffuse and unoccupied d-orbitals generate bands that are lower than the ligand's LUMO. Thirdly, the band gaps are reduced by placing strong reducing components into the

coordination sites to generate partially filled band states [117].



**Fig. 2.** Systematic band gap adjustment in MFU-4-type semiconductor. Adapted with permission [103]. Copyright 2014, Wiley-VCH.

Notably, semiconductivity in MOFs is not only identified by the band gap; rather, conductivity which increases with temperature is also considered. Due to the low charge mobility of some MOFs, those frameworks were earlier not considered as semiconductors. In recent years, an increasing number of publications on charge mobility or conductivity [118] inspired Dinca to write a review article on electronically conducting porous MOFs [119]. Also, the Dinca group synthesized a thiolated analogue of the  $M_2$ (DOBDC) series of MOFs,  $Mn_2$ (DSBDC) with a 1D Mn-S chain and reported that these MOFs have high charge mobility that is comparable to those of conventional organic semiconductors [120]. Moreso, the same research group reported a semiconducting Ni-based MOFs,  $Ni_3$ (2,3,6,7,10,11-hexaiminotriphenylene) $_2$ , having a narrow band gap and high conductivity of 0.1 eV

and  $40 \text{ S cm}^{-1}$ , respectively [121]. Their conductivity is quite high when compared to other coordination polymer and is temperature-dependent with an activation energy of approximately 0.025 eV [121]. Kitagawa and co-workers [122, 123] conducted researches on the proton conductivity of MOFs. High proton conductivity of about  $10^{-2} \text{ Scm}^{-1}$  at 85 °C and 90% relative humidity has been reported by Shimizu et al. [124]. A conductive MOF is measured by the density and mobility of charge carriers. In MOFs, the organic ligand could be the charge carrier source when the ligands are stable radicals or redox-active molecules. Also, the metal ions could be involved as charge carriers when they contain high-energy electrons or holes [119]. The incorporation of specific molecules, such as meta-sulfur chains, can enhance conductivity in MOFs [95].

Owing to the reason that MOFs are highly ordered crystal material [125], band theory, was used to study their electronic structure. The theory proposes that solids are classified according to the energy difference ( $E_g$ ) between the valence band (VB) and the conduction band (CB); metals ( $E_g < 0$  eV), semiconductors ( $0 < E_g < 3$  eV) and insulators ( $E_g > 4$  eV) [126]. However, this classification does not hold for some materials with wide orbital energy difference between the bonding atoms or low orbital overlap such as in d-electron compound, like CrO and MnO [126]. Due to the low band dispersion in MOFs, constructing conductive MOFs requires increasing the electronic coupling

between the linkers and the metal ions, thereby increasing the band dispersion.

The photon efficiencies of semiconductor MOFs are enhanced by engineering their bandgap, thereby impacting the quantum efficiency. In semiconductors, the valence and conduction bands are completely filled and empty, respectively, at absolute zero temperature, and charge separation occurs after heating [119]. The Fermi level lies in between the VB and the CB. Doping the material helps to reduce the activation energy by shifting the Fermi level nearer to the band edge of either the VB or the CB. As there is charge localization in typical MOFs, conductive MOFs are achieved by molecular doping in the pore space or introducing defects, hence, affecting the Fermi level [126]. At a given temperature, reduced activation energy results in a more significant charge density. In MOFs, the density of an electronic state near the Fermi edge is affected by the topology of the frameworks, the engineering of the metal node and the existence of unsaturated metal sites (UMS) [127]. Efficient semiconductor MOF can further be designed by turning the framework to obtain a decreased bandgap through functionalizing the linker, increasing the linker's conjugation and choosing electron-rich organic molecules or metal nodes [95].

## 2.2. Potentials, advantages and challenges of MOFs for photocatalysis

Basically, photocatalysis is a heterogeneous material, which absorbs light energy and convert it into chemical energy [128-130]. Originally, the

term photocatalysis is used in two different contexts; one is as a catalyst from the photon's point of view, which occurs when a single photon is involved in a chain reaction, thereby forming a number of product molecules [84]. The other is more commonly used and is derived from the similarity with thermal catalysis. In this photocatalytic process, a thermally inactive solid absorbs light and initiates a chemical transformation of substrates without being destroyed [84]. Photoinduced reactions are relatively more selective compared to the thermal activated system due to the reason that unwanted side reactions can be thermally inhibited. When a photocatalyst is excited upon light illumination, its reaction mechanism normally follows a single electron transfer (SET) process between the excited state and the substrate [131, 132].

Contrary to zeolites and (aluminosilicates) silicates that are UV-vis transparent in the absence of impurities, a variety of metal-organic frameworks absorb photons by their electron-rich aromatic polycarboxylate linker, followed by charge separation of the localized exciton by SET from the organic ligand to the bonding metal ions. Aromatic linkers are known for their intense absorption band (> 250 nm) and sometimes even extending into the visible region (> 400 nm), depending on the substituents [133]. The light absorption characteristics of metal-organic frameworks could be fine-tuned by accurately using suitable light-harvesting linker/components. The metal clusters which behave as semiconductor quantum dots can be constructed with visible light-responsive metal

ions like Fe [72]. Generally, the organic linkers absorb the light energy, and their light-responsive nature can be inherent depending on their functionality (like 2-aminoterephthalic acid), or the ligands can be activated through photoactive metalloligands or dyes by post-synthetic modifications (PSM) [132, 134]. Furthermore, the MOFs can be sensitized by incorporating the light-responsive component into the framework's cavities or pores. Interestingly, dual or triplet excitations at the metal node, organic ligand, and pores can be achieved in a MOF at the same time [72]. Detailed discussions on the light-responsive component of MOFs will be narrated in the subsequent section.

Unlike Zeolite, photocatalytic active sites can be easily immobilized in the linker, metal node and the cavity of MOF because of its modular nature, (combining the advantages of both inorganic and organic chemistry), thus availing it with more potential applications [14, 132]. Therefore, MOFs are more versatile than zeolites for constructing intelligent materials that can provide responses to external stimuli [93]. Another advantage of MOFs in photocatalysis is the availability of different dimensions and topologies, which encourage both the facile substrate-catalyst interactions and the size and shape selectivity during the reaction [132, 135]. The rigid and close contact of the clusters and the ligand can favor charge separation within the framework [136, 137]. Nevertheless, after the charges have been separated, charge recombination delimits the photocatalytic efficiency. Abundant with these benefits, MOFs have been photocatalytically

employed for numerous applications, such as pollution degradation [138, 139], hydrogen evolution [140], CO<sub>2</sub> reduction [31, 141] and other organic transformations [142].

One of the drawbacks of MOFs as photocatalysts is instability, both thermal and chemical [143]. Some MOFs decompose at a temperature above 250 °C coupled with the fact that their framework structure easily collapses on contact with some reagents containing strong nucleophilic species (like alkoxides and amines) and polar solvents [144]. Moreover, photochemical instability can constitute another shortcoming since the organic component of the framework can undergo some degree of photo-oxidation upon light irradiation. This oxidative degradation of the linker can be expedited by the formation of reactive species of singlet oxygen or superoxide [145, 146]. Hence cognizance of the framework stability after prolonged light irradiation should be taken. The stability after photocatalysis should be confirmed by BET surface area, XRD, and spectroscopic measurements.

### 2.3. Mechanism of CO<sub>2</sub> reduction and selectivity of the product

The linear structure of CO<sub>2</sub>, its thermodynamic stability ( $\Delta G = -400$  kJ mol<sup>-1</sup>), large electron affinity ( $-0.6 \pm 0.2$  eV) and the large energy gap between the LUMO and HOMO (13.7 eV) make it an inactive molecule [147]. Thus, converting it into value added chemicals are endothermic processes, which requires catalyst or significant input of energy [148]. Basically, for CO<sub>2</sub> to be reduced, the catalyst's/MOF's LUMO should

be above the redox potential needed for CO<sub>2</sub> reduction half reaction [102]. Photocatalytic CO<sub>2</sub> reduction is a multistep process that involves CO<sub>2</sub> adsorption, activation, dissociation of the C-O bond and the formation new C-bond [149]. As the structure of CO<sub>2</sub> bends, its LUMO level decreases [148]. The linear structure of CO<sub>2</sub> becomes bent when adsorbed on the surface of the MOFs, making it easier for the C-O bond cleavage. Fundamentally, the underlying mechanism of CO<sub>2</sub> activation and reduction involves single, double, or multiple electron transfer process [149]. The photogenerated electrons are transferred from the MOF's LUMO to CO<sub>2</sub> as shown in Fig. 3 [102, 103], thereby activating the CO<sub>2</sub> for the formation of CO<sub>2</sub><sup>-</sup> intermediate, which participate in subsequent reaction. For example, this intermediate can be protonated to HCOOH.

### Selectivity

To obtain the desired CO<sub>2</sub> reduced product, the required kinetic barrier should be overcome for the reduction process to be successful [150]. The value of the reduction potentials determines the product that would be formed. For example, as CO<sub>2</sub> reduction into formic acid requires -3.42 eV, formation of methanol needs -3.65 eV [103, 151]. Overall, CO<sub>2</sub> photoreduction is a complex reaction generating multiple products. The pathway for the photoreduction of CO<sub>2</sub> to CO and CHOOH requires relatively low kinetic barriers (two-electron process) reduction to CH<sub>3</sub>OH and CH<sub>4</sub> involves higher kinetic barriers with the transfer of 6 and 8 electrons, respectively [102], see Fig. 3.

The energy levels (HOMO and LUMO) of MOFs can be tuned to achieve the required electronic and optical response. Since MOF's LOMU and HOMO are mainly contributed by the metal cluster and the linker respectively, rational modification of these components is useful to control the product selectivity [102]. Therefore, the main product is dependent on the type/components of the MOFs.

The acidic/basic nature of metal-oxo clusters play a role on controlling the selectivity of the product during CO<sub>2</sub> reduction. As the traditional metal oxides that are basic in nature basic (MgO) forms C<sub>1</sub>-C<sub>3</sub> chain hydrocarbon product, acidic ones (SiO<sub>2</sub>) produce short chains hydrocarbons, such as methene and carbon monoxide [152]. Product selectivity of CO<sub>2</sub> photoreduction can be controlled by optimizing the major steps of CO<sub>2</sub> reduction. Photocatalysts with basic sites are more favorable since CO<sub>2</sub> adsorption on the catalyst surface is a key step in the process. Li and coworkers illustrated how the presence of alkaline metal sites (Mg<sup>2+</sup>) in CPO-27-Mg was not only beneficial for photocatalytic CO<sub>2</sub> reduction (by lowering the reaction barrier for CO<sub>2</sub> reduction), but also, changed the product selectivity [153]. Incorporating CPO-27-Mg into TiO<sub>2</sub> totally inhibited the reduction of H<sub>2</sub>O to H<sub>2</sub>, a competitive reaction of the CO<sub>2</sub> photoreduction.

Product selectivity can be influenced by the MOF's metal ion. Wang et al. evaluated the the selectivity of product and photocatalytic CO<sub>2</sub> reduction activity of three isostructural transition-metal-based MOFs (MOF-Ni, MOF-Co and MOF-

Cu) in the presence of photosensitizing [Ru(bpy)<sub>3</sub>]Cl<sub>2</sub>·6H<sub>2</sub>O and triisopropanolamine as electron donor [154]. The MOF-Ni displayed a high CO<sub>2</sub>-to-CO selectivity of 97.7%. However, MOF-Co showed a moderate CO selectivity of 47.4% while MOF-Cu exhibited high H<sub>2</sub> selectivity of 77.4%. The recorded high selectivity of MOF-Ni was attributed to the framework's low CO<sub>2</sub> reduction free energy, strong CO<sub>2</sub> binding capacity and high H<sub>2</sub> evolution reaction (side reaction). It was demonstrated that the electrons easily migrated from the Ru(bpy)<sub>3</sub>]Cl<sub>2</sub>·6H<sub>2</sub>O to the MOFs because of their matched LUMO positions [154]. Furthermore, the structure of the SBU or the arrangement of the metal ions in the SBU can affect the product selectivity as well. Two polyoxometalate-containing metalloporphyrin coordination frameworks (POMCFs), NNU-13 and NNU-14, constructed with visible-light-responsive tetrakis(4-carboxylphenyl)porphyrin (H<sub>2</sub>TCPP) linkers and Zn-ε-Keggin cluster, showed high CH<sub>4</sub> selectivity of 96.6% (surpassing all of the reported photocatalytic MOFs systems) and 96.2%, respectively, in a CO<sub>2</sub>-photoreduction system [155]. The superior selectivity was attributed to the synergistic effect of the strong reducing ability of the Zn-ε-Keggin cluster and optical/electrical properties of the TCPP group. Theoretically, the eight Mo<sup>V</sup> atoms in the cluster can donate eight electrons required for CO<sub>2</sub>-to-CH<sub>4</sub> transformation. The selectivity of the product can be controlled by integrating the framework with semiconductors, metal nanoparticles or metal ions/ heteroatom. Plasmonic nanoparticles can exhibit strong light

absorption through the collective free electron oscillations, i.e., localized surface plasmon resonances (LSPR) [152]. This enriched surface electron density can favor multielectron process for high selectivity of CH<sub>4</sub>. In addition, slow multielectron reduction process can be favored by development of heterojunctions, extending the life of the charge carriers. The LSPR effect of Au nanoparticle deposited into ZIF-67 was studied by Becerra et al. for selective light responsive CO<sub>2</sub> reduction [156]. The plasmonic Au@ ZIF-67 framework exhibited high selectivity for the photocatalytic reduction of CO<sub>2</sub> to methanol/ethanol, which was attributed to the

LSPR effect of the Au nanoparticle [156]. When Ni(TPA/TEG), with nearly 100% CO selectivity was decorated with noble metals, Ag and Rh nanocrystals, the resultant composites have a controlled photocatalytic reduction of CO<sub>2</sub> to acetic acid and formic acid [157]. Chen et al. demonstrated that adjusting the amounts of Ni<sup>2+</sup> dopants on NH<sub>2</sub>-MIL-125-Ti can affect CO selectivity [158]. They showed that the sample, NH<sub>2</sub>-MIL-125-Ni1%/Ti, doped with one percent of Ni<sup>2+</sup> ion has 98.6% CO selectivity due to enhanced charge separation and good conductivity.

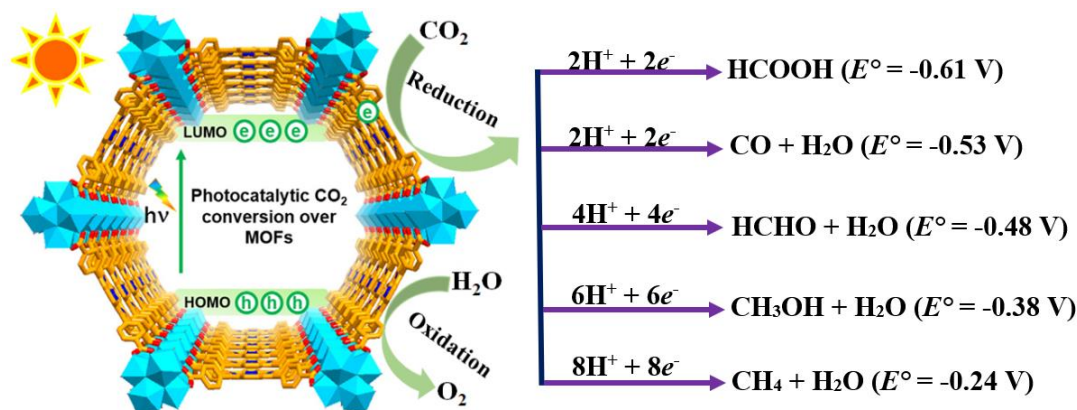


Fig. 3. Light-driven CO<sub>2</sub> reduction over MOFs in aqueous solution forming different products at various reduction potentials vs the normal hydrogen electrode (NHE). Adapted with permission [102]. Copyright 2020, Elsevier. Reproduced with permission [159]. Copyright 2019, MDPI.

### 3. Engineering the light-harvesting components of MOF

For MOFs to be active as a photocatalyst, there must be a unit of the framework that is light-responsive. Thus, engineering MOFs that originally do not absorb light to be photoactive has been achieved by immobilizing the light-responsive

component in the framework. Different components of MOFs can be tuned to be photoactive, and for a particular MOF, the component that absorbs the light affects both the mechanism and the efficiency of the MOF photocatalyst. The organic ligand, the metal clusters/SBUs, and the guests in the pores can be engineered to be visible light responsive.

### 3.1. Functionalization of organic ligands

MOFs stand as a promising material for CO<sub>2</sub> photoreduction due to their synthetic tunability and variability [160, 161]. The frameworks can be functionalized de novo, in situ, and post-synthetically, thereby availing more applicability [162-164]. The organic linkers can be rationally modified by incorporating the desired visible light functional groups that can absorb the appropriate wavelength of light, thereby enabling the photochemical reaction at the inorganic nodes [165].

The photonic efficiency of MOFs can be maximized by bandgap engineering achieved by functionalizing chromophore antenna on the MOFs backbone. Thus, the optical property of the framework will match the proper range of visible light absorption. For example, when a pending amino group is incorporated into MOF's backbone, the resultant framework exhibits an absorption band in the visible region. For MIL-125, the absorption edge was extended from 350 nm to the visible region when amino-containing ligand H<sub>2</sub>ATA, and Ti<sub>8</sub>O<sub>8</sub>(OH)<sub>4</sub>(O<sub>2</sub>CR)<sub>12</sub> clusters were used to prepare the MOFs [71]. The absorption edge of NH<sub>2</sub>-MIL-125(Ti) also extended to around 550 nm, and it is the linker H<sub>2</sub>ATA that influences the charge transfer in the TiO<sub>5</sub>(OH) clusters (Fig. 4a).

Such an enhanced visible light absorption results in an enhanced photocatalytic CO<sub>2</sub> reduction on the amino-functionalized MOF. NH<sub>2</sub>-MIL-125(Ti) generated up to 8.14 μmol of HCOO<sup>-</sup> while

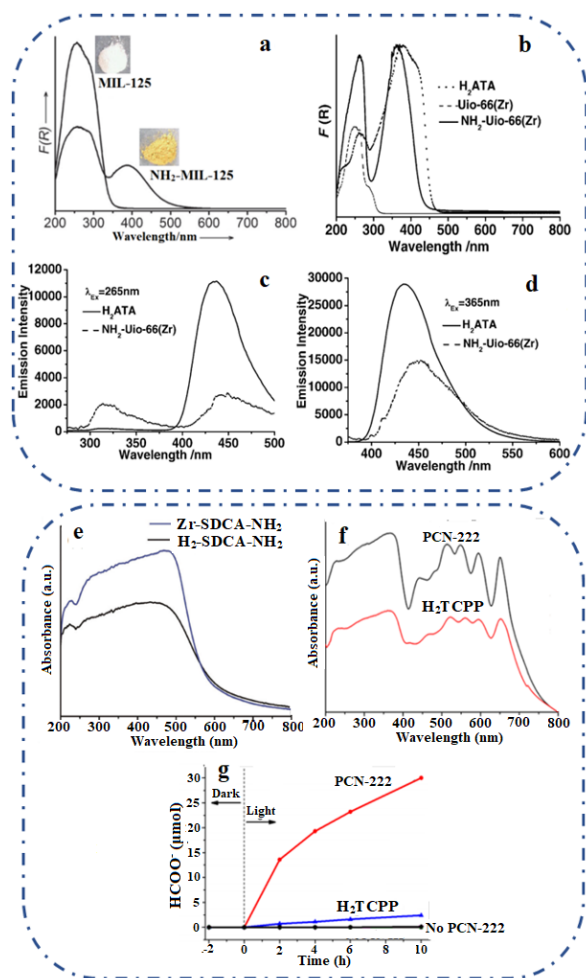
the unfunctionalized MIL-125(Ti) was not photoactive for CO<sub>2</sub> reduction under the same condition.

Li's research group used the same organic linker to construct a Zr-based MOF, NH<sub>2</sub>-UiO-66(Zr) with characteristic UV-Vis adsorption peak at about 365 nm, which is assigned to n-π\* transition of the nitrogen lone pair in the amine moiety (Fig. 4b) [80]. However, the band at about 265 nm for the ligand is due to the π-π\* transition. The MOFs recorded intense adsorption at 265 nm due to the overlap of the ligand's π-π\* transition and that of the metal cluster. Photoluminescence (PL) analysis was applied to disclose that there were electron transfers from the excited linker to the Zr-oxo cluster in the MOFs. Excitation of the linker (H<sub>2</sub>ATA) by 265 nm light, resulted in a PL band at 450 nm, while two PL bands at 314 and 450 nm occurred for the MOFs, Fig. 4c. The lower band intensity observed at 450 nm for the amine functionalized UiO-66(Zr) is due to the charge transfer from the ligand to the metal node.

As shown in Fig. 4d, further excitation of the ligand at 365 nm resulted to band at 434 nm, but the intensity of the peak for the NH<sub>2</sub>-UiO-66(Zr) decreased because of the same electron transfer from the excited amine linker to the Zr nodes. Since the linker was not active for CO<sub>2</sub> reduction, then the activity of the MOFs emerged from the interaction between the metal node and the linker, thereby confirming the result reported above for NH<sub>2</sub>-MIL-125(Ti) [80].

The synergy between highly conjugated molecules and the amine group is established as a





**Fig. 4** (a) Light adsorption spectra of the two MIL-125(Ti) MOFs (b) spectra of H<sub>2</sub>ATA and UiO-66(Zr) based MOFs (c) photoluminescent properties of H<sub>2</sub>ATA and NH<sub>2</sub>-UiO-66 at 265 nm and 365 nm (d) excitation wavelengths. Reproduced with permission [69]. Copyright 2013, Wiley-VCH. (e) light adsorption spectra of H<sub>2</sub>SDCA-NH<sub>2</sub> and Zr-SDCA-NH<sub>2</sub>, Reproduced with permission [139]. Copyright 2018, The Royal Society of Chemistry, and (f) The spectral properties of H<sub>2</sub>TCPP and PCN-222, (g) Catalytic performance of PCN-222, Reproduced with permission [141]. Copyright 2015, American Chemical Society.

feasible approach to improve the light absorption capacity of MOF-based photocatalyst. Besides the abovementioned examples, [Zr<sub>6</sub>O<sub>4</sub>(OH)<sub>4</sub>(L)<sub>6</sub>·8DMF; H<sub>2</sub>L = 2,2'-diamino-

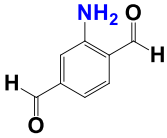
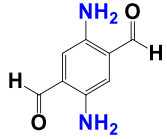
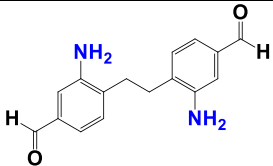
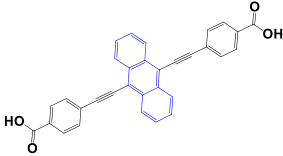
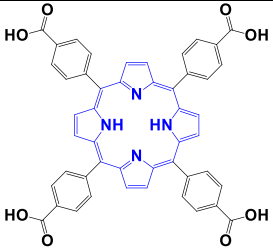
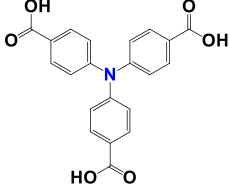
4,4'-stilbene dicarboxylic acid) exhibited a considerable absorption edge around 600 nm, Fig. 4e [166]. The HCOO<sup>-</sup> formation rate of 96.2 μmol h<sup>-1</sup> mmol MOF<sup>-1</sup> was recorded for [Zr<sub>6</sub>O<sub>4</sub>(OH)<sub>4</sub>(L)<sub>6</sub>·8DMF, which is appreciably high when compared to other NH<sub>2</sub> functionalized Zr-containing MOFs. In addition, an anthracene-based organic ligand with large conjugacy was used to construct NNU-28, which exhibited great potential to reduce CO<sub>2</sub> to HCOO<sup>-</sup> with high efficiency [167]. With a visible light adsorption of 650 nm, the frameworks generated formate at rate of 183.3 mmol h<sup>-1</sup> mmol MOF<sup>-1</sup>. The high catalytic activity was due to the combined effect from the Zr<sub>6</sub>-oxo cluster and the anthracene-based linker.

Moreover, porphyrin-based frameworks were exploited for visible light photocatalytic CO<sub>2</sub> reduction [168]. Fig. 4f. showed that tetrakis(4-carboxyphenyl)-porphyrin (H<sub>2</sub>TCPP) has intense absorption in the 200 - 800 nm region. Under visible light, the porphyrin-based [169] MOF selectively adsorb and reduce CO<sub>2</sub> to produce 30 μmol of HCOO<sup>-</sup> anion in 10 h, (Fig. 4g) which is much higher than the activities reported over MIL-125-NH<sub>2</sub> and UiO-66-NH<sub>2</sub> under similar condition [71, 80]. Notably, the catalyst is highly selective for HCOO<sup>-</sup> anion production, since no other product was detected. The steady-state PL measurement illustrates that assembling the H<sub>2</sub>TCPP into zirconium-porphyrin MOF, results in higher PL emission quenching. Both ultrafast spectroscopy and time-resolved PL spectroscopy confirmed the emergence of a type of deep electron trapping state in porphyrin-based MOFs, which hinders the



recombination of electrons and holes, thus enhancing the CO<sub>2</sub> photoreduction efficiency [168]. Structural representations of light-harvesting linkers are illustrated in **Table 1**.

**Table 1** Light harvesting ligands and catalytic performance.

Acronym Name/ Empirical formula	Light harvesting ligands	Catalytic Active Site	Performance	Ref.
1) NH <sub>2</sub> -MIL-125(Ti) Ti <sub>8</sub> O <sub>8</sub> (OH) <sub>4</sub> (bdc-NH <sub>2</sub> ) <sub>6</sub>		TiO <sub>5</sub> (OH)	1) I. 8.14 mmol HCOO <sup>-</sup> in 10 h	[71]
Pure and mixed ligand NH <sub>2</sub> -UiO- 66(Zr)		Zr <sub>6</sub> O <sub>4</sub> (OH) <sub>4</sub>	I. pure NH <sub>2</sub> -UiO-66(Zr) 13.2 mmol; II. mixed ATA and 2,5- diaminoterephthalic acid (DTA): 20.7 mmol HCOO <sup>-</sup> in 10 h	[80]
Zr-SDCA-NH <sub>2</sub> , ([Zr <sub>6</sub> O <sub>4</sub> (OH) <sub>4</sub> (L) <sub>6</sub> ] <sub>8</sub> - DMF		Zr <sub>6</sub> O <sub>4</sub> (OH) <sub>4</sub>	96.2 μmol h <sup>-1</sup> mmolMOF <sup>-1</sup>	[166]
NUU-28		Zr <sub>6</sub> O <sub>4</sub> (OH) <sub>4</sub>	183.3 mmol h <sup>-1</sup> mmolMOF <sup>-1</sup>	[167]
PCN-222, MOF- 545 or MMPF-6, Zr <sub>6</sub> (μ <sub>3</sub> -OH) <sub>8</sub> (OH) <sub>8</sub> - (TCPP) <sub>2</sub>		Zr <sub>6</sub> O <sub>4</sub> (OH) <sub>4</sub>	30 μmol of HCOO <sup>-</sup> in 10 h	[168]
Gd-TCA		Fe-Fe hydrogenase, Ni(Cyclam) complexes	quantum yield of about 0.21% for CO <sub>2</sub> reduction	[170]

### 3.2. Bandgap engineering

An increase in the concentration of an active light-responsive component, like NH<sub>2</sub> moieties in the linker of a framework, promotes the

photocatalytic activity of NH<sub>2</sub>-based MOFs. Improved light absorption and further shift to the visible region were obtained when the linker, ATA, was mixed with the two amino-containing linker, 2,5-diaminoterephthalate (DTA) [80]. Fig. 5a

revealed that the spectrum of the mixed linker MOF,  $\text{NH}_2\text{-UiO-66(Zr)}$ , had a shift to the visible region compared to the parent MOFs. Consequently, the mixed  $\text{NH}_2\text{-UiO-66(Zr)}$  produced 20.7  $\mu\text{mol}$  of formate while  $\text{NH}_2\text{-UiO-66(Zr)}$  generated 13.2  $\mu\text{mol}$  after reacting for 10 h. Thus, an increase in amino functionality reduces the bandgap and improves the photocatalytic  $\text{CO}_2$  reduction. Through experimental and computational approaches, Hendon et al., explored band gap modification of titanium-containing MIL-125 by examining the detailed electronic structure of the aminated linkers (Fig. 5b) frameworks [171]. They elucidated the exact role of the amine group in lowering the band gap of MIL-125- $\text{NH}_2$ . It was confirmed that the observed decrease in band gap (from 3.6 eV for MIL-125 to 2.6 eV for  $\text{NH}_2\text{-MIL-125}$ , Fig. 5c) was due to electron transfer from the 2p N orbital to the benzene ring, thus resulting in a higher red-shifted band than the VB edge of MIL-125 [171]. Precisely, the presence of  $\text{NH}_2$  increases the VB by 1.2 eV, without affecting the energy level of the CB. By simulation, they further controlled the optical response of the  $\text{bdc}(\text{NH}_2)_2$  (diaminated linker) and other functionalities like -OH, -Cl and  $-\text{CH}_3$ . The  $\text{bdc}(\text{NH}_2)_2$  linker lowered the band gap of MIL-125 by 1.28 eV, Fig. 5d.

A mixed ligand strategy was further applied to enhance the activity of mixed metal (Zr/Ti) node MOFs [172]. Moreover, adding diamine-substituted ligand provided broader light absorption coverage for the frameworks, as depicted in Fig. 5e. The diaminated MOFs achieve better charge separation; thus, it accepts more

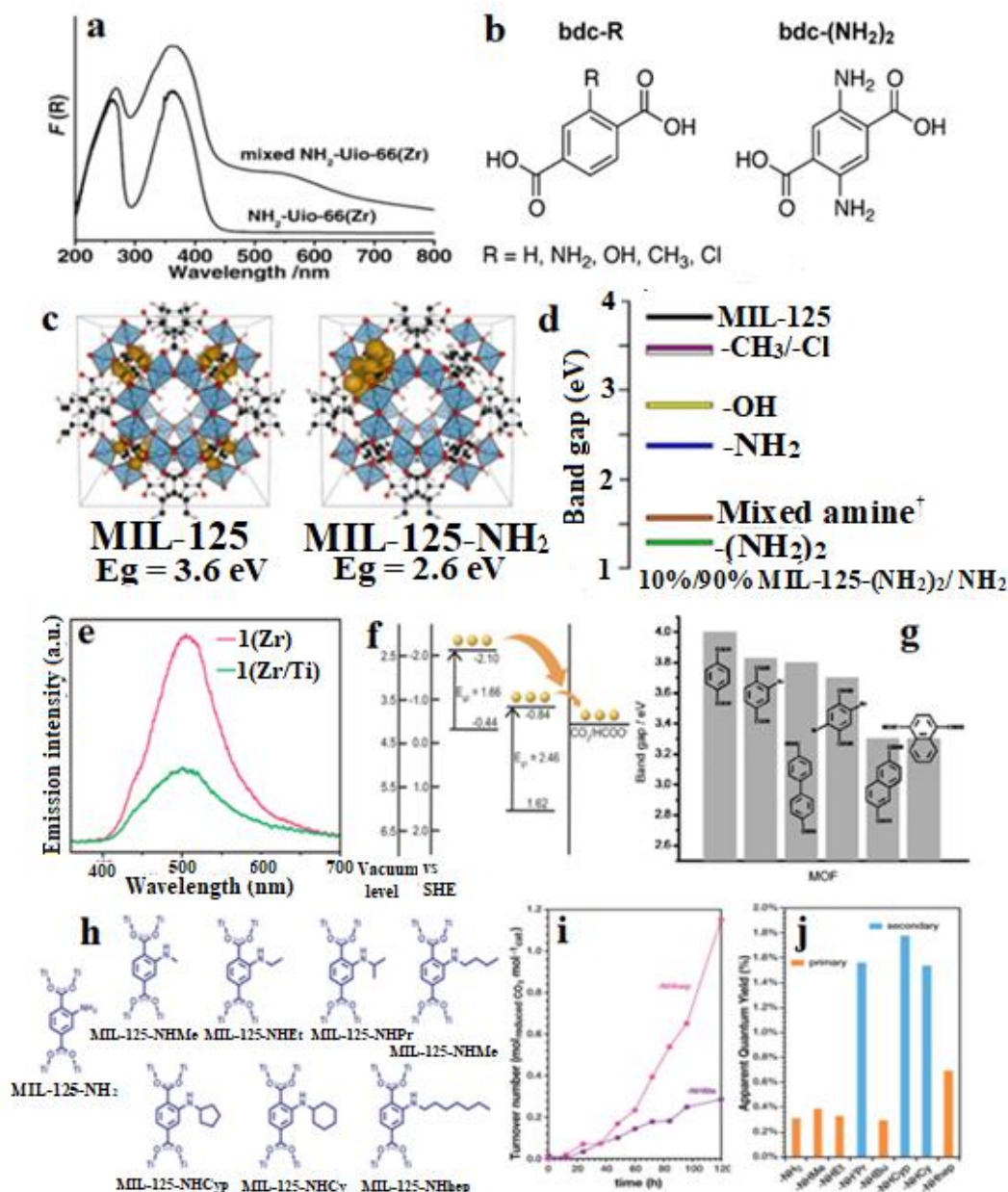
electrons from the linker to reduce  $\text{CO}_2$  than single amine-containing MOFs, Fig. 5f. Band gap energy of isorecticular MOFs can be fine-tuned by varying the organic linker, as illustrated by Gascon et al. in 2008, Fig. 5g [173]. They reported that the effect of the linker could be related to the resonance effect and the photocatalytic activities of these frameworks vary with their band gap.

Based on the aforementioned result, Uribe-Romo and coworkers investigated the effect of varying the chain length (from methyl to heptyl as shown in Fig. 5h) and connectivity (primary and secondary) of the 2-aminoterephthalate organic linker that features N-alkyl group on light-induced  $\text{CO}_2$  reduction [174]. Hypothetically, due to subtle inductive effects, the sequential addition of carbon atoms to the N-alkyl amino group leads to larger electron density around the nitrogen atom, resulting in increased density in the terephthalate ring [174]. Consequently, the top of the valence band will be successively destabilized, causing a decrease in the bandgap of the framework and increment in photocatalytic activity.

The optical bandgaps of the Ti-based MOFs reduced, attributed to the inductive donor nature of the alkyl substituent, thus displaying higher catalytic activities. Fig. 5j illustrates that the secondary N-alkyl substitution has a higher apparent quantum yields than that of the primary N-alkyl analogs, assigned to longer-lived excited-state. Precisely, cyclopentyl-containing MOF, MIL-125-NHCyp has smaller bandgap, long-life excited state and larger apparent quantum yield of  $E_g = 2.29$  eV,  $\tau = 68.8$  ns, and  $\Phi_{\text{app}} = 1.80\%$

respectively, compared to the values for MIL-125-NH<sub>2</sub>  $E_g = 2.56$  eV,  $\tau = 12.8$  ns, and  $\Phi_{app} = 0.31\%$  [174]. During photoreduction, the rate-determining

step is the extent of electron transfer from excited Ti<sup>3+</sup> to CO<sub>2</sub>



**Fig. 5.** (a) Light spectrum of the NH<sub>2</sub>-Uio-66(Zr) (single and mixed linker). Reproduced with permission [78]. Copyright 2013, Wiley-VCH. (b) Structural representation of substituted bdc ligands (c) Band gap of MIL-125 and NH<sub>2</sub>-MIL-125, (d) Band gaps of functionalized MIL-125. Reproduced with permission [144]. Copyright 2013, American Chemical Society. (e) PL of Zr/Ti bimetallic MOFs, (f) Band structure of Zr/Ti bimetallic MOFs. Reproduced with permission [145]. Copyright 2015, The Royal

Society of Chemistry. (g) Band gaps of isorecticular MOFs with different linkers. Adapted with permission [146]. Copyright 2008, Wiley-VCH. (h) Structural representation of the organic linkers in MIL-125-NH<sub>2</sub> and various N-substituted isorecticular MOFs, (i) Catalytic performance of MIL-125-NHMe and MIL-125-NHhep, (j) The apparent quantum yield over isorecticular MIL-125-NHR MOFs. Adapted with permission [147]. Copyright 2017, The Royal Society of Chemistry

### 3.3 Introducing metal complexes as bridging ligand

Although metals and metal oxide complexes are endowed with superior efficiency for CO<sub>2</sub> photoreduction, however, it is still difficult to control them at the molecular level [175-177]. The application of this class of molecular catalysts is also limited by insufficient activity due to the catalyst poisoning by dimerization and low solubility of substrates and catalysts [178]. In the light of this situation, enhanced activity of these molecular catalysts can be achieved by tethering their metal complexes within MOFs' backbone, thereby spatially isolating the molecular catalyst [179]. Taking advantage of the intrinsic characteristics of MOFs; a high surface area that enables more areal density of active sites, transparent single crystal materials with easy light penetration and facile access of substrate to active sites, the backbone of MOFs are considered as a most appropriate host for anchoring selective molecular catalyst [178, 180]. Therefore, MOF-based multi-component photocatalytic systems constructed by metal

complex bridging linkers have been designed to achieve synergetic catalytic effects.

In 2011, Lin and coworkers designed a stable Zr-based MOF photocatalyst by introducing a metal complex as a light-harvesting center [181]. They used a mix-and-match synthetic approach to tether Re-containing complex into a UiO-67 framework, and the as-synthesized MOFs shows selective CO<sub>2</sub> conversion into CO using triethylamine as electron donor. Although the homogeneous molecular Re<sup>I</sup>(bpy)(CO)<sub>3</sub>Cl (bpy=2,2'-bipyridine) complex has been widely reported as a very active and selective CO<sub>2</sub> reduction catalyst, it degrades easily because of dimerization. Anchoring this complex on the framework's backbone makes the catalytic center site-isolated, which prevents quick degradation by dimerization. Under visible light radiation, a TON of 10.9 in 20 h was obtained, which is almost three times higher than that of the Re(bpy)(CO)<sub>3</sub>Cl homogeneous complex system, Fig. 6a [181]. Recently, Choi and co-workers heterogenized the same photocatalytic molecular complex by incorporating it into a framework structure for CO<sub>2</sub> reduction [182].

Lin and coworkers [183] further constructed MOFs photocatalyst by more elongated dicarboxylate ligand containing (bpy)Re(CO)<sub>3</sub>Cl complex and Zr<sub>6</sub>(μ<sub>3</sub>-O)<sub>4</sub>(μ<sub>3</sub>-OH)<sub>4</sub> clusters, which is a single site photocatalyst for the conversion of CO<sub>2</sub> to CO and HCOO<sup>-</sup>. The CO<sub>2</sub> reduction process by unimolecular reaction mechanism due to the site isolation of the immobilized catalyst. The isolated catalytic site enables to study the selectivity of the catalyst and the unimolecular mechanistic pathway, thereby circumventing the parallel bimolecular pathway in the homogeneous system. Although the TON for CO (6.4 in 6 h) is higher than that of the homogenous catalysts, this MOF catalyst decomposes during the catalytic reaction because of the partial hydrogenation of the bpy followed by Re decomplexation.

Since not every photon absorbed by these metal-complexed MOFs is utilized for photocatalysis, the quantum yields of those MOF systems are usually low. Enhancement in the quantum yield can be realized by introducing additional molecular photosensitizers into the frameworks. A Zr-based MOF containing the manganese complex, Mn(bpydc)-(CO)<sub>3</sub>Br (bpydc = 5,5'-dicarboxylate-2,2'-bipyridine) as the organic bridging linker, was constructed by Cohen and coworkers [184]. To enhance the quantum

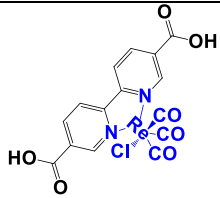
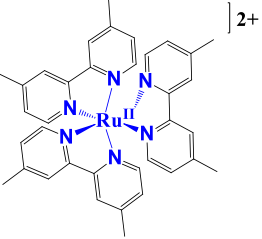

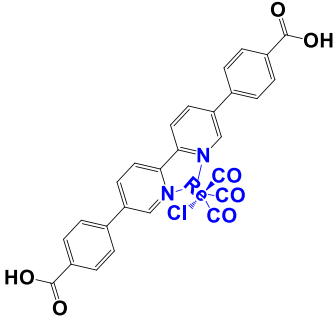
yield, [Ru(4,4'-dimethyl-2,2'-bipyridine)<sub>3</sub>]<sup>2+</sup> and 1-benzyl-1,4-dihydronicotinamide were immobilized into the framework as photosensitizer and sacrificial reductant, respectively. The resultant UiO-67-Mn(bpy)(CO)<sub>3</sub>Br is selective and active and for visible-light CO<sub>2</sub> reduction to formate. A turnover number of about 110 in 18 h was recorded for the Mn-catalyst incorporated MOF system. The increased activity was assigned to the struts providing isolated Mn-based active sites, thus inhibiting the dimerization of the singly reduced Mn-catalyst (Fig. 6b). Notably, due to the introduction of the Ru-photosensitizer, the recorded high quantum yield of  $\Phi_{\text{formate}} = 13.8\%$  in the visible region exceed not only those of Mn(bpydc)(CO)<sub>3</sub>Br and Mn(bpy)(CO)<sub>3</sub>Br homogeneous analogues, but also many precious-metal containing MOF [184].

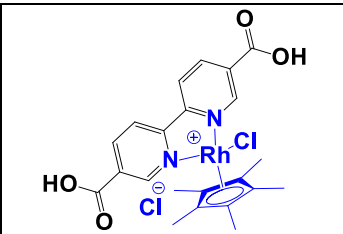
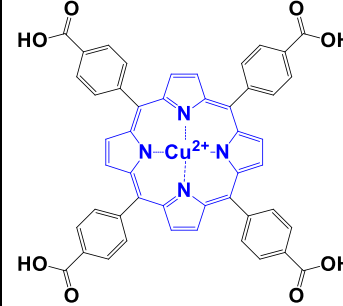
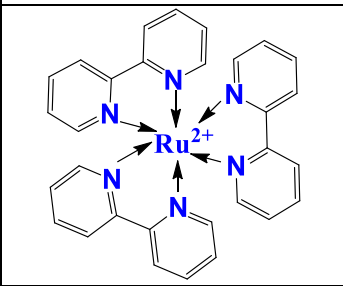
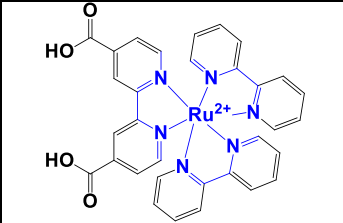
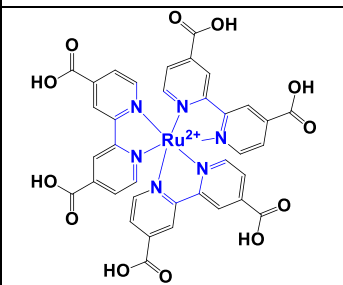
The post-synthetic ligand exchange method, Fig. 6c, can be employed to effectively heterogenize a rhodium photosensitizer, [Ru(bpy)<sub>3</sub>]Cl<sub>2</sub> (bpy=2,2'-bipyridine), into a MOF framework, forming rhodium-functionalized MOF, Cp\*Rh@UiO-67. This Ru-functionalized MOF is active for the reduction of CO<sub>2</sub> into formate [185]. With an optimal molar Rh loading of around 10%, the MOF-based system is more stable and selective than the homogeneous analogue.

The post-synthetic ligand exchange approach, as shown in **Scheme 1**, can be employed to effectively heterogenize a rhodium photosensitizer,  $[\text{Ru}(2,2'\text{-bipyridine})_3]\text{Cl}_2$ , into a MOF framework, forming rhodium-functionalized MOF,  $\text{Cp}^*\text{Rh@UiO-67}$ . This Ru-functionalized MOF is active for the reduction of  $\text{CO}_2$  into formate [185]. With an optimal molar Rh loading of around 10%, the MOF-based system is more selective and stable than the homogeneous analogue. Recently, Mellot-Draznieks and coworkers used a highly porous inert  $\text{MIL-101-NH}_2(\text{Al})$  as a nanoreactor by irreversible co-immobilization of catalytic

$[\text{Cp}^*\text{Rh}(4,4'\text{-bpydc})]^{2+}$  and light-responsive  $[\text{Ru}(\text{bpy})_2(4,4'\text{-bpydc})]^{2+}$  into a framework structure for  $\text{CO}_2$  reduction, Fig. 6d [186]. Unlike their Ru-Rh homogeneous reaction counterpart that generates  $\text{H}_2$  as the main product, this Rh-Ru@MIL-101- $\text{NH}_2$  system has a good selectivity for reducing  $\text{CO}_2$  into formate without any trace of  $\text{CO}$  or  $\text{H}_2$ . Therefore, through inhibition of proton reduction, the MOF host has the potential to alter the selectivity of a reduction reaction. The structures of light-harvesting metal complexes, together with their performance for  $\text{CO}_2$  reduction, are illustrated in **Table 2**.

**Table 2** Light harvesting metal complexes

Acronym Name/ Empirical formula	Metal complexes	Catalytic Active Site	Performance	Ref.
$\text{Zr}_6\text{O}_4(\text{OH})_4(\text{bpdc})_6$ , UiO-67		$\text{Zr}_6\text{O}_4(\text{OH})_4$	TON of 10.9 in 20 h	[181]
UiO-67 $\text{Mn}(\text{bpy})(\text{CO})_3\text{Br}$			TONs for formate reached 110 18 h	[184]
$\text{Zr}_6(\text{O})_4(\text{OH})_4$ - $[\text{Re}(\text{CO})_3\text{Cl}(\text{bpydb})]_6$		$\text{Zr}_6(\mu_3\text{-O})_4(\mu_3\text{-OH})_4$	6.4 TONs for $\text{CO}$ in 6 hours	[183]

Cp*Rh@UiO-67		Zr <sub>6</sub> O <sub>4</sub> (OH) <sub>4</sub>	125 TON formate in 10 h	[185]
(H <sub>2</sub> TCPP[Al(OH)] <sub>2</sub> (DMF <sub>3</sub> - (H <sub>2</sub> O) <sub>2</sub> ) Or Al-PMOF (denoted as SCu)		Al(OH)O <sub>4</sub>	262.6 ppm g <sup>-1</sup> h <sup>-1</sup> of methanol	[187]
Co <sub>6</sub> -MOF		Co <sub>6</sub> (μ <sub>3</sub> -OH) <sub>6</sub>	39.36 μmol CO under 3 hours	[188]
Ru-Rh@MIL-101- NH <sub>2</sub> (Al)		[Cp*Rh(4,4'- bpydc)] <sup>2+</sup>	0.33 μmole/mg of formate in 5 h	[186]
Cd <sub>3</sub> [Ru- L1] <sub>2</sub> ·2(Me <sub>2</sub> NH <sub>2</sub> ) [Ru(5,5'-dcbpy) <sub>3</sub> ] <sup>4-</sup> ([Ru-L1] <sup>4-</sup> , 5,5'-dcbpy = 2,2'-bipyridine- 5,5'-dicarboxylate)		Cd-O cluster	16 μmole of formate in 6 h	[189]

A high nuclearity Co<sup>II</sup> clusters-based MOF (Co<sub>6</sub>-MOF) recorded CO<sub>2</sub> adsorption capacity of 55.24 cm<sup>3</sup> g<sup>-1</sup>. This framework can work synergistically with a ruthenium-based photosensitizer, [Ru(bpy)<sub>3</sub>]Cl<sub>2</sub>·6H<sub>2</sub>O (bpy = 4,4'-bipyridine), for the conversion of CO<sub>2</sub> to

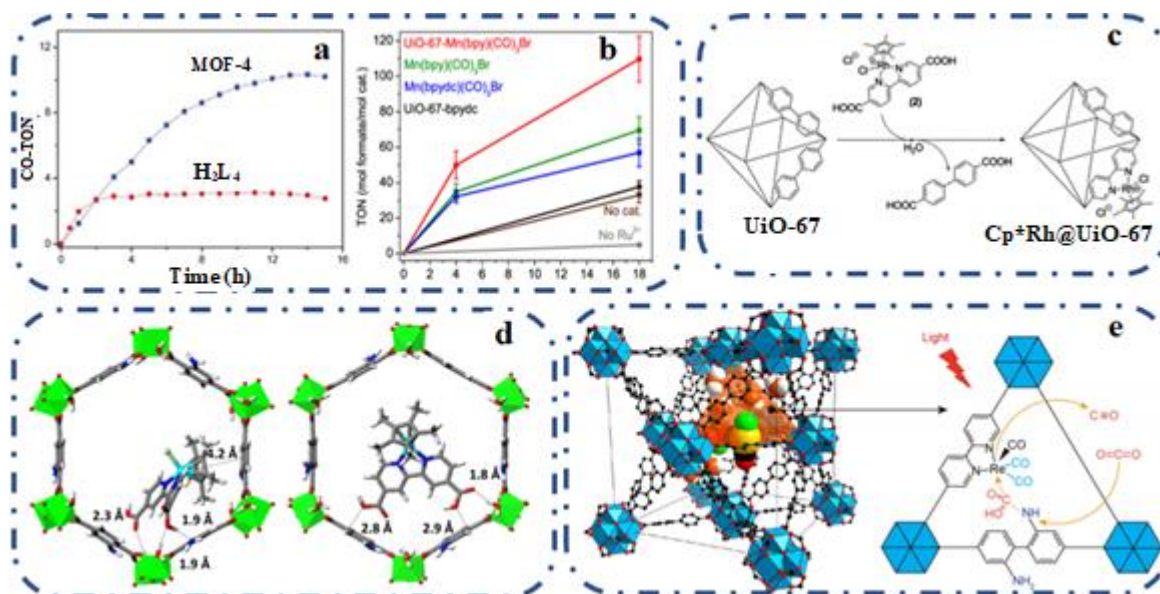
CO under [188]. This porous material can generate 39.36 μmol of CO under 3 hours of visible light irradiation. Based on theoretical calculation studies, the excited electrons from the LUMO of the Ru-based photosensitizer can be easily transferred to the LUMO of the Co<sub>6</sub>-



MOFs, which facily activate the adsorbed  $\text{CO}_2$  and then enhance the reduction reaction activity [188]. In another work, Co-thiolate units were post-synthetically immobilized into Zr-based frameworks to prepare Zr-DMBD-Co MOF (DMBD=2,5-dimercapto-1,4-benzenedicarboxylate) solids, which show high selectivity and photocatalytic  $\text{CO}_2$  conversion into CO. Up to 98% CO selectivity was recorded and the TON reach as high as 97 941 [190]. Moreover, the fine balance in the proximity of  $(\text{Re}^{\text{I}}(\text{CO})_3(2,2'\text{-bipyridine-5,5'}$ -dicarboxylate)(Cl) and  $-\text{NH}_2$  containing

ligands was synthetically adjusted to fabricate a molecular MOF photocatalyst, Re-MOF- $\text{NH}_2$ , with high activity and selectivity (Fig. 6e) [191].

The maximum catalytic activity of the framework was achieved at 33 % mole, when the ratio of  $\text{NH}_2$  functionality was varied from of  $\text{NH}_2$  functionality from 0 to 80 mol%. The results from the extended X-ray absorption and *in-situ* IR showed that after introducing  $\text{NH}_2$  moieties, the Re-CO bond of the metal complex split into asymmetric bonds of 2.3Å and 1.4Å with different



**Fig. 6** (a) Photocatalytic performance of MOF-4 and homogeneous  $\text{H}_2\text{L}_4$ . Reproduced with permission [154]. Copyright 2011, American Chemical Society. (b) Plot of formate turnover number during  $\text{CO}_2$  photocatalysis experiments for Zr-based MOFs. Reproduced with permission [157]. Copyright 2015, American Chemical Society. (c) Heterogenization of a rhodium complex into UiO-67 framework. Adapted with permission [158]. Copyright 2015, Wiley-VCH. (d) Two different DFT simulated geometry for the Rh-complex immobilized in MIL-101- $\text{NH}_2(\text{Al})$ . Adapted with permission [159]. Copyright 2018, Wiley-VCH. (e) The structure of  $-\text{NH}_2$  functionalized Re-MOF and the mechanism for  $\text{CO}_2$  conversion. Adapted with permission [164]. Copyright 2017, Nature Publishing Group.



CO<sub>2</sub> vibrations. Consequently, the carbonyl groups acquire an asymmetric configuration, which aids the formation of CO<sub>2</sub> intermediates. The asymmetric carbonyl groups and the intermolecular stabilization of carbamate intermediates resulted in a 3-fold increment in the photocatalytic reduction of CO<sub>2</sub> into CO. Also, Sun et al. [192] demonstrated that the CO<sub>2</sub> reduction performance of MOF-253 can be improved by incorporating photosensitizing Ru carbonyl complex, Ru(bpy)<sub>2</sub>Cl<sub>2</sub>, into the material.

The linking units of MOFs that mimic the natural light-harvesting complexes can be immobilized in MOFs photocatalytic systems. Different porphyrins based metal complexes have been applied as catalysts for photocatalytic CO<sub>2</sub> reduction in homogenous systems [193-196], due to the versatile functionality, selective adsorption [197] and strong light harvesting [198] and unique nature of porphyrin ligand [199]. Therefore, modifications of porphyrin-based MOFs for photocatalysis gained recent attention [200-202]. For example, the CO<sub>2</sub> reduction to CH<sub>3</sub>OH activity for a porphyrin-based MOF modified with Cu<sup>2+</sup> showed improvement by up to 7 times, as compared with the counterpart without Cu<sup>2+</sup> modification [187].

A series of Zr polyphenolate-decorated-(metallo)porphyrin MOFs, ZrPP-*n*-M (*n* = 1 for THPP = 5,10,15,20-tetrakis(3,4,5-trihydroxyphenyl)porphyrin, *n* = 2 for THBPP = 5,10,15,20-tetrakis(3,4,5-trihydroxybiphenyl)porphyrin, M = H<sub>2</sub>, Zn, Cu, Fe, Co) were constructed with the eclipsed porphyrin

arrays linking with the Zr-oxide node to form an extended porous frameworks [203]. Interestingly, ZrPP-1 can withstand unprecedented pH stability over a wide range (pH = 1, HCl and concentrated NaOH solution ≈ 20 M). The cobalt-metalated analog, ZrPP-1-Co, with uniform distributed active centers, recorded not only a high CO<sub>2</sub> adsorption capacity (≈90 cm<sup>3</sup> g<sup>-1</sup> at 1 atm, 273 K), but also high reduction of CO<sub>2</sub> into CO over CH<sub>4</sub> (≈14 mmol g<sup>-1</sup> h<sup>-1</sup>) under visible-light irradiation without the support of any cocatalyst. The porphyrins absorb incident photons, transfer the electrons to the Co<sup>2+</sup> and with the aid of TEOA, Co<sup>2+</sup> is reduced to Co<sup>+</sup> and then to Co<sup>0</sup>, which activate CO<sub>2</sub> for the reduction process [203].

Yang et al. prepared an Eu-Ru(phen)<sub>3</sub>-MOF (phen = phenanthroline) by incorporating a photosensitizing Ru(phen)<sub>3</sub>-derived tricarboxylate ligand into Eu-MOF with a SBUs containing Eu<sub>2</sub>(μ<sub>2</sub>-H<sub>2</sub>O) [204]. Transient absorption and theoretical calculations were used to unveil that the photo-generated electrons were transferred from the from Ru metalloligands into the node to generate dinuclear [EuII-H<sub>2</sub>O-EuII]-active sites, which participate in two-electron photoreduction of CO<sub>2</sub> to HCOOH with a rate of 321.9 μmol h<sup>-1</sup> mmolMOF<sup>-1</sup>.

Through rational design of framework structures at atomic level, the recombination of electron-hole pairs can be suppressed. Thus, a pyrazolyl-porphyrinic based MOF, PCN-601, composed of catalytic Ni-oxo cluster and light-responsive metalloporphyrin ligands linked via pyrazolyl groups, demonstrated efficient CO<sub>2</sub>-

photoreduction [205]. The larger  $\pi$ -conjugation pyrazolyl groups caused higher  $\pi$ -d orbital overlaps with Ni-oxo cluster and their robust coordination spheres endowed the frameworks with proper energy band alignment (efficient charge separation) and ultrafast ligand-to-node electron transfer. Hence, the CO<sub>2</sub>-to-CH<sub>4</sub> production rate (10.1  $\mu\text{mol}\cdot\text{h}^{-1}\cdot\text{g}^{-1}$ ) of this pyrazolyl-porphyrinic Ni-MOF surpass 3 times (PCN-222) and 17 times (Ni<sub>3</sub>TCPP) higher than those of analogous carboxyl porphyrinic MOFs and inorganic Pt/CdS photocatalyst.

### 3.4. Activation of metal nodes

Light-responsive metal ions for the construction of the secondary building unit of MOFs is an interesting strategy to activate the metal nodes for enhanced photocatalytic activity. Li's research group constructed different Fe-based MOFs, including, MIL-53(Fe), MIL-88B(Fe) and MIL-101(Fe) together with their amino-functionalized derivatives [72]. Due to the presence of Fe-O clusters, the three parent MOFs are visible light responsive. Upon excitation, electrons transferred from O<sup>2-</sup> to Fe<sup>3+</sup>; hence the unfunctionalized Fe-containing MOFs are active for CO<sub>2</sub> reduction, Fig. 7, which was not possible with both MIL-125(Ti) and UiO-66(Zr) [72]. For the three unfunctionalized MOFs, MIL-101(Fe) recorded the highest HCOO<sup>-</sup> production (59.0  $\mu\text{mol}$  in 8 h),

attributable to the presence of more coordinated unsaturated Fe metal sites.

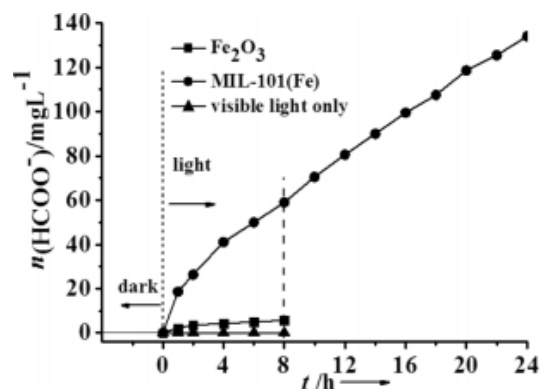


Fig. 7. Catalytic performance of MIL-101(Fe). Reproduced with permission from Ref. 70. Copyright 2014, American Chemical Society

### 3.5. Mechanisms of light-harvesting and electron transfer

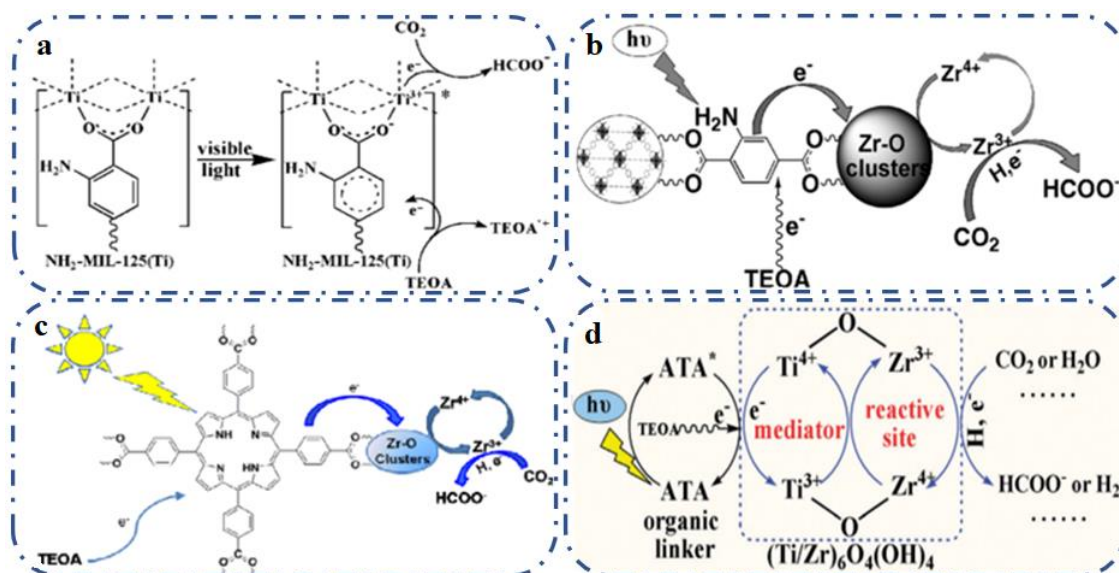
The light-responsive component of MOFs influences the overall electron transfer mechanism of the frameworks. When the organic ligands harvest light, and the excited electrons are transferred from the ligand to the metal nodes; the phenomenon is called a linker-to-metal cluster charge transition (LCCT) mechanism. It results to charge separation state in the framework, which is similar to the features of metal oxide semiconductors, supporting the semiconductor-like behavior of MOFs [206]. Most MOF photocatalysts undergo the LCCT mechanism. Fu et reported that when NH<sub>2</sub>-MIL-125(Ti) was irradiated with visible light, the amino functionality in the

ligand absorbs the light and transfers electrons to  $\text{Ti}^{4+}$  through the O in the  $\text{TiO}_5(\text{OH})$  cluster [71]. Consequently,  $\text{Ti}^{4+}$  is reduced to  $\text{Ti}^{3+}$ , whereas TEOA acts as sacrificial electron donor and further provides a basic environment to facilitate the reduction. Thus, the photocatalytic pathway follows the LCCT mechanism as illustrated in **Scheme 1a** [71]. ESR and UV-DR spectra were used to confirm the existence of  $\text{Ti}^{3+}$  in the metal nodes. The participation of  $\text{Ti}^{3+}$  in the  $\text{CO}_2$  reduction was revealed in the analysis of the green suspension formed upon visible light irradiation in  $\text{N}_2$  environment. Garcia and co-workers further confirmed the generation of  $\text{Ti}^{3+}$  when they characterized the transient states generated upon the excitation of  $\text{NH}_2\text{-MIL-125}(\text{Ti})$  with light [207]. The studied transient signal is compatible with photoinduced charge separation with the generation of electrons and holes.

It was further demonstrated that the LCCT mechanism occurs in  $\text{NH}_2\text{-UiO-66}(\text{Zr})$  (Scheme 1b) [80]. Similarly, on irradiation of visible light, the excited  $\text{ATA}^*$  transfers electrons and reduce  $\text{Zr}^{4+}$  to  $\text{Zr}^{3+}$ , which subsequently reduces  $\text{CO}_2$  to  $\text{HCOO}^-$ . ESR

spectroscopy was used to ascertain that a signal with a g value of 2.002, which increases with irradiation time, occurs, and this signal disappears when  $\text{CO}_2$  is introduced into the system (Fig. 8a and b). This signal was not observed upon visible light irradiation of both  $\text{UiO-66}(\text{Zr})$  and  $\text{H}_2\text{ATA}$ . Consequently, there was photogeneration of  $\text{Zr}^{3+}$  intermediates which were involved in the  $\text{CO}_2$  reduction of over the Zr-MOFs [80].

Electron spin resonance measurements were conducted to examine the mechanism of  $\text{CO}_2$  reduction over PCN-222. The results support that  $\text{Zr}^{3+}$  intermediates are formed when photoexcited electrons are transferred from the ligand,  $\text{H}_2\text{TCPP}$ , to the Zr-O clusters in the presence of TEOA as electron donor Scheme 1c [168]. Notably, Ti-substituted  $\text{NH}_2\text{-UiO-66}(\text{Zr}/\text{Ti})$ , i.e., bimetallic assembly, transfers electrons to  $\text{Zr}^{4+}$  through a Ti-mediated electron transfer mechanism as shown in Scheme 1d.[208] The excited SBU generated is  $(\text{Ti}^{3+}/\text{Zr}^{4+})_6\text{O}_4(\text{OH})_4$  since  $\text{Ti}^{4+}$  can easily accept electrons from the organic linkers than the  $\text{Zr}^{4+}$  centers. The  $[\text{Re}^{\text{I}}(\text{CO})_3(\text{dcbpy})\text{Cl}]$  ( $\text{H}_2\text{L}_4$ ) derivatized MOF **4** photocatalytic  $\text{CO}_2$  reduction followed a metal-to-ligand charge

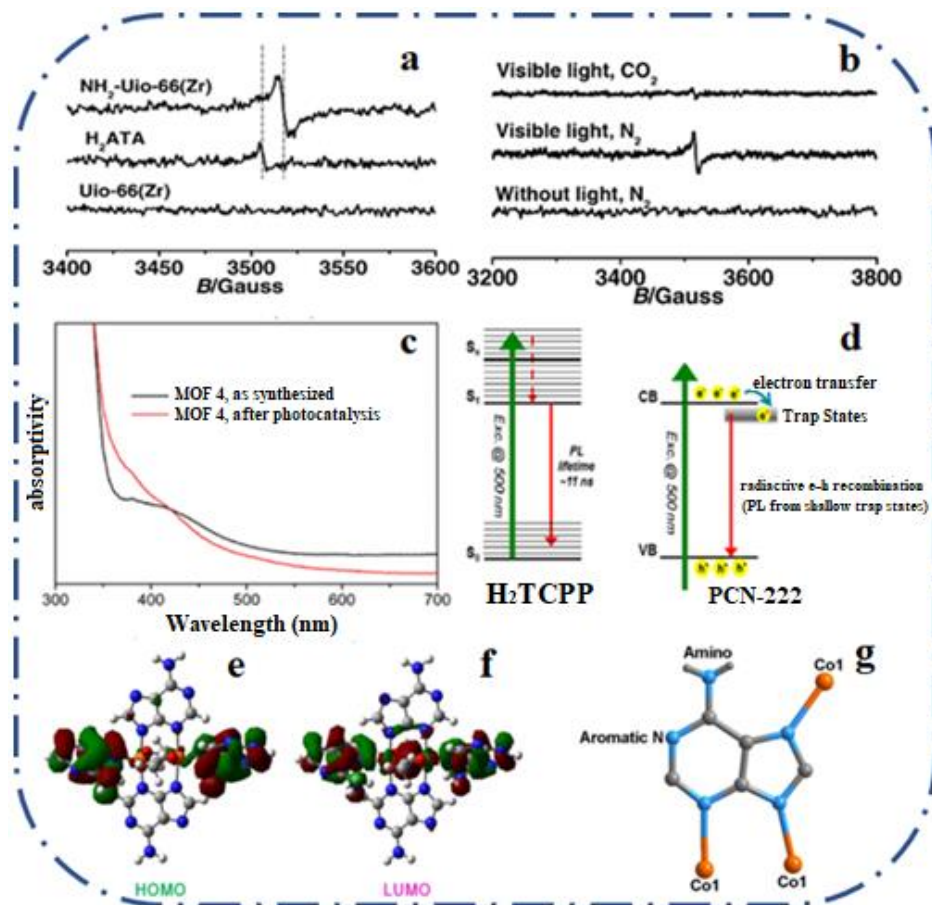


**Scheme 1.** LCCT mechanism for the visible light-induced reduction of  $\text{CO}_2$  over (a)  $\text{NH}_2\text{-MIL-125(Ti)}$ , Adapted with permission [69]. Copyright 2012, Wiley-VCH. (b)  $\text{NH}_2\text{-UiO-66(Zr)}$ . Reproduced with permission [78]. Copyright 2013, Wiley-VCH. (c)  $\text{PCN-222}$ , Adapted with permission [141]. Copyright 2015, American Chemical Society, and (d)  $\text{NH}_2\text{-UiO-66(Zr/Ti)}$ . Reproduced with permission [178]. Copyright 2015, The Royal Society of Chemistry.

transfer (MLCT) mechanism [181]. On recycling the MOF **4**, the recovered solid was inactive for CO generation; thus, there is detachment of Re-carbonyl moieties (i.e., up to 43.6% of Re was leached into solution) from the dcbpy group in the MOFs that results in the loss of the peak at 412 nm. Notably, the disappearance of the peak confirmed the MLCT absorption properties of the  $\text{Re}(\text{CO})_3(\text{bpy})\text{Cl}$  species, as presented in Fig. 8c.

By combining the advantages of ZIF-9 for  $\text{CO}_2$  capture and the catalytic function of cobalt and imidazolate in  $\text{CO}_2$  reduction catalysis, a

MOF-photocatalyst that was induced by visible light excitation of dye molecules was obtained. There was no metal-to-ligand charge transfer in the Co-ZIF-9 framework [209]. For MOFs/semiconductor composites, photogeneration of electrons and holes occurs at the semiconductor accompanied by the transfer of electrons to the  $\text{CO}_2$  reduction site. Wang et al. showed that upon visible light illumination on Co-ZIF-9/CdS composite, the electron-hole pairs were produced on the CdS, followed by migration of the  $e^-$  to the CB of the CdS semiconductor [210].



**Fig. 8.** (a) Electron spin resonance spectra of NH<sub>2</sub>-Uio-66(Zr), Uio-66 MOFs and H<sub>2</sub>ATA, and (b) the spectra of NH<sub>2</sub>-Uio-66(Zr) at different conditions. Reproduced with permission [78]. Copyright 2013, Wiley-VCH. (c) UV-Vis spectra of MOF 4. Reproduced with permission [154]. Copyright 2011, American Chemical Society. (d) Electron transfer mechanisms in H<sub>2</sub>TCPP and PCN-222. Reproduced with permission [144]. Copyright 2015, American Chemical Society. Electrons distribution on HOMO (e) and LUMO (f) orbitals. and (g) the coordination environment for the biological adenine molecule in biomimetic MOF structures. Reproduced with permission [183]. Copyright 2019, Wiley-VCH.

Furthermore, the photocatalytic mechanism over M/NH<sub>2</sub>-MIL-125(Ti) (M=Pt and Au) shows that upon light illumination, the excited ATA linkers transfer electrons through the M-N bond to the noble metal nanoparticles which trap some of the electrons to provide redox reaction sites and can also hinder

electron-hole recombination [211, 212]. On the mechanistic viewpoint for the H<sub>2</sub>TCPP MOF, the 500 nm photons initiate electron transition from the ground state to the excited state followed by deactivation to the lowest-lying excited state, as illustrated in Fig. 8d [168]. Thus, PL of around 11 ns was detected. For the

PCN-222 system, two distinct lifetimes exist for the PL emission (around 712 nm), which shows that the recombination of electron-hole originates from two trap states that are close to the conduction band bottom. Thus, the two trap states inhibit recombination [168].

Photocatalytic CO<sub>2</sub> reduction in MOFs can also occur on the organic linker only without the involvement of the traditional metal center; thus, no LCCT or MLCT mechanism occurs in these systems. Thus two green biomimetic MOFs, [Co<sub>2</sub>(HAD)<sub>2</sub>(AD)<sub>2</sub>(BA)]·DMF·2H<sub>2</sub>O (**ADMOF-1**; HAD = adenine and BA = butanedioic acid) and [Co<sub>2</sub>(HAD)<sub>2</sub>(AD)<sub>2</sub>(IA)<sub>2</sub>]·DMF (**AD-MOF-2**; IA = isobutyric acid) were constructed and employed as photocatalyst for the conversion of CO<sub>2</sub> to formic acid [213]. Here, both the excitation and the CO<sub>2</sub> reduction process are solely nucleobase adenine-dependent without any participation of the Co-oxo clusters. The active CO<sub>2</sub> adsorption and activation sites were confirmed by DFT calculation, which unveiled that the adsorbed CO<sub>2</sub> at the metallic site would escape quickly due to its saturated coordination sphere. Therefore, this metallic unit is not the active site of the biomimetic MOFs. As demonstrated in Fig. 8e and Fig. 8f, the calculated electron density distribution revealed that the electron density on the LUMO and HOMO orbitals of the frameworks are

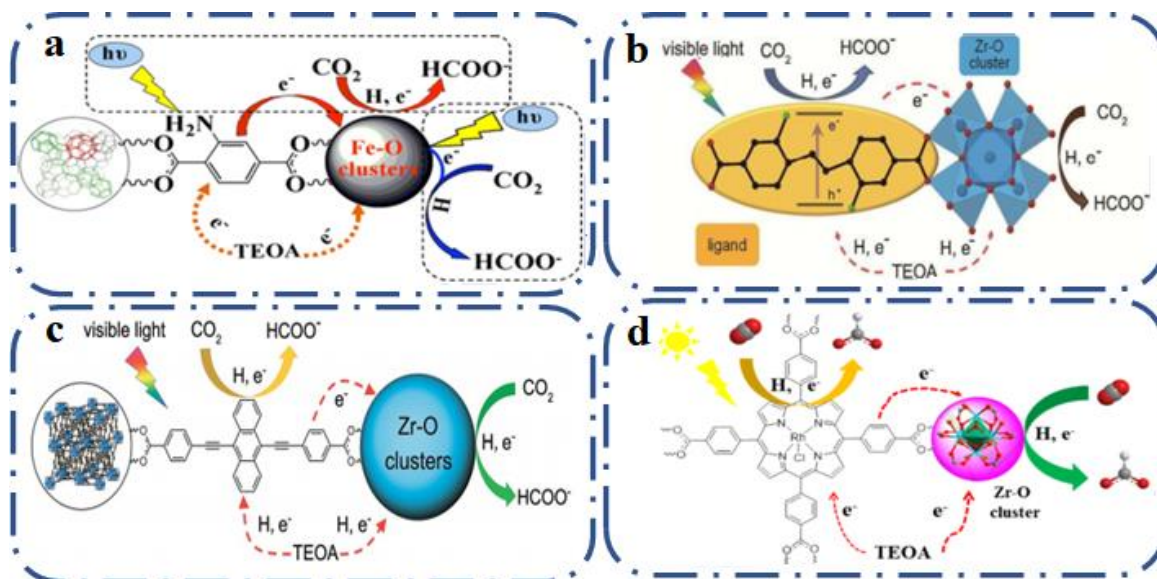
mainly localized on the adenine molecule [213].

Thus, upon light irradiation, photoexcited electrons are generated on biological adenine molecules (Fig. 8g) where the active site is the *o*-amino assisted naked aromatic nitrogen atom via the strong binding with the activated CO<sub>2</sub> intermediate for subsequent CO<sub>2</sub>-to-HCOOH conversion. Interestingly, in pure aqueous solution, **AD-MOF-2** recorded formic acid generation rate of 443.2 μmol g<sup>-1</sup> h<sup>-1</sup> [213].

The aforementioned mechanisms are based on excitation at a single component of the framework, like the ligand, additives/dyes, or the metal complex, thereby following a single excitation pathway. Nevertheless, excitations both at the ligand and the metal nodes of a MOF termed "dual excitation pathways" have been reported [72]. The cooperative effect of dual excitation pathways significantly enhances their CO<sub>2</sub> reduction activities. For an amine-containing ligand, the dual excitation pathways consist of; excitation of amine group, followed by an electron transfer to the metal cluster which is also excited by photons. Wang et al. reported that the photoreduction of CO<sub>2</sub> by series of NH<sub>2</sub> based MIL-(Fe) MOFs are based on a dual excitation mechanism which comprises; excitation of amine moiety followed by transfer of electron to the Fe-oxo cluster by

LCCT mechanism, couple with the direct excitation of Fe–O clusters (**Scheme 2a**) [72]. They used the wavelength dependence of the of NH<sub>2</sub>-MIL-101(Fe) and MIL-101(Fe) to elucidate the mechanism for the improved catalytic activity over the modified MOF. Sun et al. further reported a dual excitation mechanism by showing that the ligand, H<sub>2</sub>SDCA-NH<sub>2</sub> (2,2'-diamino-4,4'-stilbene dicarboxylic acid) can absorb visible light to sensitize the Zr<sub>6</sub>-O cluster via the LMCT and then the CO<sub>2</sub> photoreduction process occurs at this metal clusters, **Scheme 2b** [166]. Moreover, the excited H<sub>2</sub>SDCA-NH<sub>2</sub> can, on its own, directly reduce CO<sub>2</sub> to formate. The mechanism for the NNU-28 is by dual

photocatalytic routes of the Zr<sub>6</sub>-oxo clusters by the LMCT process and generation of photoinduced charges by radical formation on the anthracene-based ligand, 4,4'-(anthracene-9,10-diylbis(ethyne-2,1-diyl))dibenzoic acid scheme 2c [167]. Moreover, rhodium(III)-porphyrin-based MOFs (Rh-PMOF-1(Zr)) with a dual catalytic center has been reported, Scheme 2d.[214] The rhodium-porphyrin ligand on its own can act as an active center and carry out the CO<sub>2</sub> reduction process. On the other hand, the metalloporphyrin ligand can also absorb light in the visible region and further transfer the electrons to the Zr-O nodes, where the CO<sub>2</sub> reduction process occurs.



**Scheme 2.** (a) Dual excitation mechanism over amino-containing MOFs with Fe-oxo cluster. Adapted with permission [70]. Copyright 2014, American Chemical Society. (b) Zr<sub>6</sub> oxo cluster and H<sub>2</sub>SDCA-NH<sub>2</sub> ligand. Reproduced with permission [139]. Copyright 2018, The Royal Society of Chemistry. (c) anthracene-based ligand and Zr<sub>6</sub> oxo cluster and rhodium-porphyrin



ligand. Adapted with permission [140]. Copyright 2016, The Royal Society of Chemistry. and (d)  $Zr_6$  oxo cluster. Reproduced with permission [184]. Copyright 2018, Elsevier.

#### 4. Improving the charge dynamics of MOF photocatalysts

The activities of MOF-photocatalysts are hindered by inefficient transfer of an electron between the frameworks and the homogeneous component and slow mass transport through the channel of the MOFs. Thus, most of these catalysts need the incorporation of some components in order to achieve a significant  $CO_2$  reduction. Of importance is the precise assembling of different functionalities in a single MOF structure, thereby generating a multicomponent MOF that is efficient for artificial photosynthesis.

##### 4.1. Plasmonic Enhancement by Metal loading

Generally, the loading of noble metals into semiconductors is a known means to hinder the recombination of light-induced charge carriers [215, 216]. Sun et al. first reported the effect of noble metal on the photocatalytic performance of MOF-based photocatalyst [211]. They prepared Pt and Au-doped  $NH_2$ -MIL-125(Ti) photocatalyst for the  $CO_2$  reduction to  $HCOO^-$  under the irradiation of visible light. Both formate and hydrogen are produced over noble metal incorporated  $NH_2$ -MIL-125(Ti), whereas only formate was generated over pure  $NH_2$ -

MIL-125(Ti). In 8 h, about 40.2 and 235 mmol of  $H_2$  was respectively produced over Au/ and Pt/ $NH_2$ -MIL-125(Ti). The evolution indicates that the noble metal facilitates electron transfer from the linker to the noble metal nanoparticles, knowing that noble metals are good electron traps and can offer suitable redox reaction sites for  $H_2$  evolution [211]. For  $CO_2$  reduction to formate, the two co-catalysts behaved differently, compared with the parent MOF. The Au-doped MOF showed lower activity to form formate (about 9.06 mmol in 8 h), while 10.75 mmol is generated over non-modified  $NH_2$ -MIL-125(Ti), thus there was about 16 % decrease in the activity. The Pt-loaded sample exhibit an unusual enhancement of activity, generating about 12.96 mmol of formate which is about 21 % increment as compared to the parent MOF [211].

Furthermore, insufficient electron transfer between the visible light-responsive molecular catalyst and the MOFs catalyst (SBUs), are optimized by integrating the whole catalytic system within one material [178, 217]. Yaghi and coworkers [218] demonstrated a MOF-coated nanoparticle photocatalyst with two different functional units for enhanced  $CO_2$  reduction activity. The Zr-MOF, UiO-67 ( $Re_n$ -MOF), was constructed by attaching the active

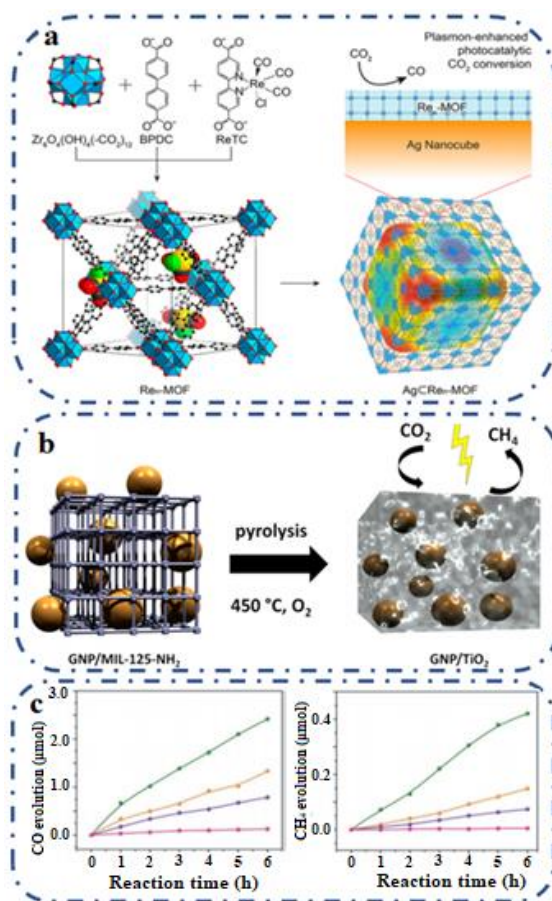


$\text{Re}^{\text{I}}(\text{CO})_3(\text{BPYDC})\text{Cl}$  complex, BPYDC = 2,2'-bipyridine-5,5'-dicarboxylate in the linker as illustrated in Fig. 9a. The density of the complex in the framework was systematically controlled to establish an optimum combination, with  $\text{Re}_3$ -MOF having the highest activity. For the cooperatively improved photocatalytic activity to be attained, there should be a fine balance of proximity between the numbers of Re complexes per unit cell [218]. Thus, they established that the trend of the activity results from the molecular environment within the framework which varied with photoactive centers' density. Importantly, after coating the optimal  $\text{Re}_3$ -MOF frameworks onto Ag, the light-responsive Re centers were evenly confined to the near-surface electric fields at the Ag nanocubes' surface, thereby resulting in 7-fold catalytic enhancement conversion of  $\text{CO}_2$  to CO with stability up to 48 h [218]. The precision and systematic variation applied in the design of the catalysts, together with the interfacial spatial resolution with plasmonic nanostructures, contributes to their unique improved performance.

As presented in Fig. 9b, MIL-125 composed of Ti-oxo clusters as SBUs was employed as sacrificial precursors to fabricate GNP/ $\text{TiO}_2$  material by disassembling the GNP/ $\text{NH}_2$ -MIL-125 through pyrolysis [219].

The hybrid composite materials show significant UV light promoted  $\text{CO}_2$  reduction to  $\text{CH}_4$  when compared to pristine samples such as AuROlite ( $\text{Au}/\text{TiO}_2$ ) and P-25. The incorporation of gold nanoparticles (GNP) on the MOF-derived  $\text{TiO}_2$  material enhanced their  $\text{CO}_2$  reduction performance. The hybrid material acts as a support matrix for the dispersion and stabilization of small gold nanoparticles, which are well-dispersed on its outer surface.

An atomically dispersed catalyst comprising single metal atom tethered on MOFs to maximize the atom efficiency is another strategy to improve the efficiency of MOF-photocatalyst for  $\text{CO}_2$  reduction. Ye and co-workers [220] incorporated Co (unsaturated single atoms) in MOF-525, i.e.  $\text{Zr}_6\text{O}_4(\text{OH})_4(\text{TCPP-H}_2)_3$ , TCPP=4,4',4'',4'''-(porphyrin-5,10,15,20-tetrayl) tetrabenzoate, to optimize the selective capture and photocatalytic  $\text{CO}_2$  reduction capacity of the MOFs under the irradiation of visible light. Based on the mechanistic studies, the single Co atoms deeply boost the efficiency of the charge separation, and the migration of the electrons from the porphyrin to Co sites leads to the generation of long-lived electrons for the reduction process. Consequently, the MOF-525-Co catalyst exhibit highest  $\text{CH}_4$  and CO production rate of 36.76 and



**Fig. 9.** (a) Structural representation of Re-MOF and Ag@Re-MOF for plasmon-enhanced photocatalytic  $\text{CO}_2$  reduction. Reproduced with permission [188]. Copyright 2016, American Chemical Society. (b) Fabrication of GNP/TiO<sub>2</sub> from GNP/NH<sub>2</sub>-MIL-125 by pyrolysis. Reproduced with permission [189]. Copyright 2015, American Chemical Society. (c) CO and CH<sub>4</sub> evolution performance of H<sub>6</sub>TCPP, MOF-525-Zn (purple), MOF-525-Zn (orange) and MOF-525-Co (green). Reproduced with permission [190]. Copyright 2016, Wiley-VCH.

$200.6 \mu\text{mol g}^{-1} \text{h}^{-1}$  respectively, under the irradiation of light for 6 hours, much higher than the value for MOF-525-Zn ( $\text{CH}_4$ ,  $11.635 \mu\text{mol g}^{-1} \text{h}^{-1}$ ;  $\text{CO}$ ,  $111.7 \mu\text{mol g}^{-1} \text{h}^{-1}$ ) and MOF-525 ( $\text{CH}_4$ ,  $6.2 \mu\text{mol g}^{-1} \text{h}^{-1}$ ;  $\text{CO}$ ,  $64.02 \mu\text{mol g}^{-1} \text{h}^{-1}$ ) as presented in Fig. 9c.[220] Concisely, MOF-525-Co shows a respective equivalent enhancement of up to 5.93-fold and 3.13-fold in CH<sub>4</sub> and CO evolution, compared to the parent MOF-525.

#### 4.2. MOFs based composite photocatalysts

MOF-based composite material,  $\text{Cd}_{0.2}\text{Zn}_{0.8}\text{S}@ \text{UiO}-66-\text{NH}_2$ , was constructed by Su et al. for  $\text{CO}_2$  reduction [221]. It was unveiled that the efficient charge separation and transfer on the interface between UiO-66-NH<sub>2</sub> and  $\text{Cd}_{0.2}\text{Zn}_{0.8}\text{S}$  contributed to the improved performance of the hybrid structure when compared with pristine components. At 20 wt% UiO-66-NH<sub>2</sub> content, the  $\text{CH}_3\text{OH}$  generation rate of  $6.8 \text{ mol h}^{-1} \text{ g}^{-1}$  was recorded. In addition,  $\text{Zn}_2\text{GeO}_4/\text{Mg}-\text{MOF}-74$  composite showed 7 times higher photocatalytic  $\text{CO}_2$  conversion into CO than the pristine  $\text{Zn}_2\text{GeO}_4$  attributed to reduced electron-hole recombination [222]. PL and EIS measurements confirmed the improved charge-transfer feature of the composite. The combined effect of the two materials induces

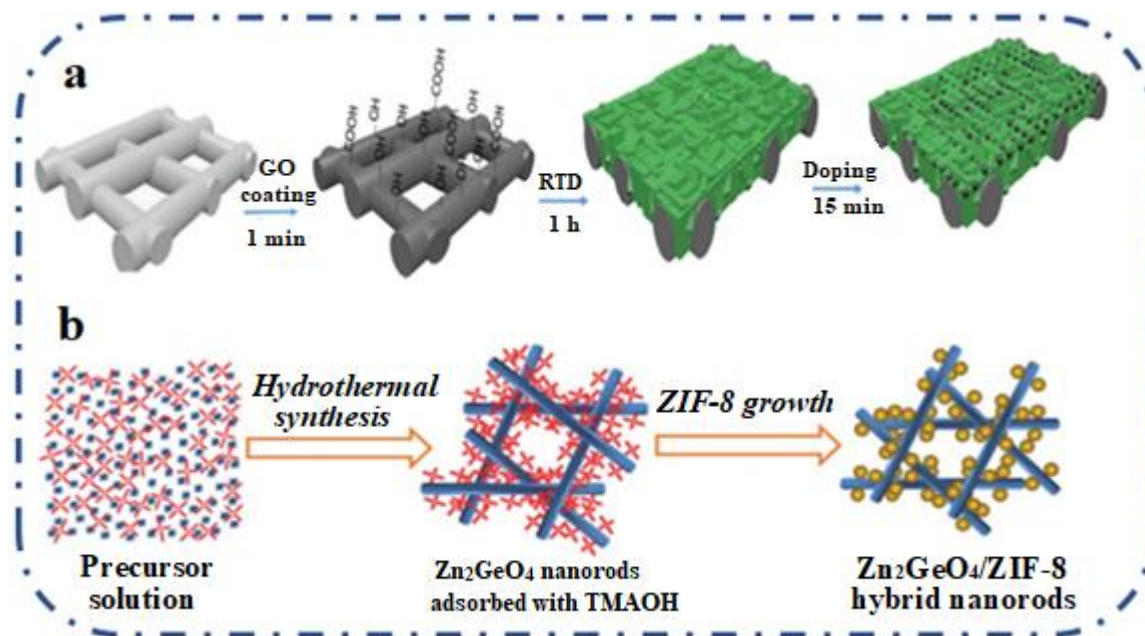
an effective electron transfer from  $\text{Zn}_2\text{GeO}_4$  to  $\text{Mg}^{2+}$ , thus enhancing the performance.

A zirconium-based MOF coupled with carbon nitride nanosheets (CNNS), UiO-66/CNNS hybrid structure was electrostatically self-assembled, taking advantage of negatively and positively charged CNNS and UiO-66, respectively [223]. The electron-hole pair recombination in CNNS is suppressed in the composite because of the facile electron transfer from the CNNS to the UiO-66. Consequently, UiO-66/CNNS shows a higher catalytic activity than CNNS. Two different photoactive inorganic semiconductors can be loaded on MOFs to improve their photocatalytic activity. Yu et al. incorporated *g*- $\text{C}_3\text{N}_4$  nanocrystals and CdTe quantum dots on  $\text{NH}_2$ -UiO-66 to form  $\text{NH}_2$ -UiO-66/*g*- $\text{C}_3\text{N}_4$ /CdTe composites that can, under visible-light irradiation, convert  $\text{CO}_2$  to  $\text{HCOOH}$  with a generation rate of  $24.6 \mu\text{mol g}^{-1} \text{h}^{-1}$ , outperforming  $\text{NH}_2$ -UiO-66 by 7.5 fold higher [224].

Also, Maina and coworkers employed a rapid thermal deposition (RTD) synthetic approach to achieve a controllable thin-film encapsulation of  $\text{TiO}_2$  and  $\text{Cu-TiO}_2$  within ZIF-8 membranes for efficient  $\text{CO}_2$  conversion under UV irradiation, Fig. 10a [225]. It was realized that  $\text{CH}_3\text{OH}$  and  $\text{CO}$  were the only products formed with the yield depending on

the concentration of dopant semiconductor particles. The best activity was obtained with 7  $\mu\text{g}$  loading of  $\text{Cu-TiO}_2$ , promoting the  $\text{CO}$  and  $\text{CH}_3\text{OH}$  yields of the pristine ZIF-8 membrane by 233 % and 70 %, respectively. Moreover, a ZIF-67 nanotube was employed as a precursor to prepare  $\text{Co}_{1.11}\text{Te}_2$  material that is half-metallic in nature and exhibits high photocatalytic performance for  $\text{CO}_2$  conversion. XPS analysis and DFT calculations were used to confirmed the half-metallic character of the fabricated material, thereby improving its electron transferability [226].

Ultrafast spectroscopy was used to show that excited electrons can be transferred from an inorganic semiconductor to MOF, which not only suppresses the charge recombination in the semiconductor but at the same time, supply energetic electrons to reduce the adsorbed  $\text{CO}_2$  on the MOF.[217] This concept is illustrated by coating a  $\text{TiO}_2$  onto  $\text{Cu}_3(\text{BTC})_2$  (HKUST-1) to generate a core-shell  $\text{Cu}_3(\text{BTC})_2@ \text{TiO}_2$  structure for  $\text{CO}_2$  photoreduction. The composite exhibits a five-fold reduction of  $\text{CO}_2$  to  $\text{CH}_4$  compared to pristine  $\text{TiO}_2$ . Both transient photocurrent response measurements and incident-photon-to-current conversion efficiency (IPCE) characterizations were used to verify the improved charge-separation performance of the catalyst [217].



**Fig. 10** (a) The assembly of semiconductor nanoparticles doped MOF membranes. Adapted with permission [195]. Copyright 2017, American Chemical Society. (b) Synthetic pathway of Zn<sub>2</sub>GeO<sub>4</sub>/ZIF-8 hybrid nanorods. Reproduced with permission [201]. Copyright 2013, The Royal Society of Chemistry.

The effect of Co-ZIF-9 as a cocatalyst for CO<sub>2</sub> photoreduction was also demonstrated for other semiconductor photocatalyst systems. For example, realizing the co-catalytic property of Co-ZIF-9, a high visible-light photocatalytic semiconductor, CdS was integrated with Co-ZIF-9 to generate a system capable of reducing CO<sub>2</sub> [210]. At 420 nm monochromatic irradiation, an apparent quantum yield of 1.93% was reached. Both photocurrent generation and in-situ PL measurements were used to confirm the role of Co-ZIF-9 for promoting electron transfer. Also, the strong interaction between CdS and MIL-101(Cr) in the CdS/MIL-101(Cr),

promoted the electron-hole pairs transfer efficiency of the composite, which exhibited an improved CO<sub>2</sub> reduction under visible light [227]. Wang and coworkers reported that Co-ZIF-9 can function as a MOF-containing cocatalyst for CO<sub>2</sub> photoreduction [209]. This Co-based MOF cocatalyst can cooperate well with a ruthenium-based photosensitizer, [Ru(bpy)<sub>3</sub>]Cl<sub>2</sub>·6H<sub>2</sub>O (bpy = 2,2'-bipyridine), along with TEOA as an electron donor. Irradiation of visible-light on the ternary system resulted in the conversion of CO<sub>2</sub> into CO at a rate of 1.4 μmol min<sup>-1</sup>, giving rise to a catalytic TON of about 450 within 2.5 hours under mild reaction conditions [209]. In

contrast, in the absence of either the dye or Co-ZIF-9, no reaction occurred, and CO production was hindered significantly.

A Gb-based MOF as a visible-light photosensitizer was constructed by assembling a triphenylamine moiety [170]. Moreover, redox cocatalysts (Fe-Fe hydrogenase and the Ni(Cyclam) complexes) with suitable redox potential were incorporated into the pores of the frameworks; thus, the close confined proximity between the cocatalysts and the photosensitizer facilitate the effective electron transfer [228]. Therefore, the assembled artificial photosynthetic systems present efficient photocatalytic CO<sub>2</sub> reduction and H<sub>2</sub> evolution. In addition, loading lead halide perovskite (LHP) quantum dots (QDs) on MOFs can facilitate charge separation efficiency, thereby improving the catalytic CO<sub>2</sub> photoreduction. In this regard, Lu and coworkers encapsulated low-cost CH<sub>3</sub>NH<sub>3</sub>PbI<sub>3</sub> (MAPbI<sub>3</sub>) perovskite quantum dots (QDs) on the pores of Fe-porphyrin-containing frameworks, whose performance is 38 times higher than its analogue without the QDs [229].

A similar idea was also demonstrated by integrating a metal-free light harvester, graphitic carbon nitride (g-C<sub>3</sub>N<sub>4</sub>), with a Co-ZIF-9, which functions as a cocatalyst [230]. The CO<sub>2</sub> reductions were carried out in the

presence of bipyridine as a secondary electron mediator and TEOA in a mild reaction condition (30 °C and 1 bar CO<sub>2</sub>). In situ PL measurements were used to elucidate the synergistic charge-mediating effects in the presence of Co-ZIF-9 and bpy, which can inhibit the recombination of charge carriers in the g-C<sub>3</sub>N<sub>4</sub> semiconductor [230]. In this stable semiconductor–redox system, the photochemical CO<sub>2</sub> reduction was induced by the visible light excitation of the g-C<sub>3</sub>N<sub>4</sub> semiconductor as a solar energy transducer. Either bpy or Co-ZIF-9 can suppress the quenching of the photoexcited charges in the system.

Liu et al. reported a semiconductor-MOF nanocomposite, ZIF-8/Zn<sub>2</sub>GeO<sub>4</sub> hybrid nanorods, fabricated by growing ZIF-8 nanoparticles on the surface semiconducting Zn<sub>2</sub>GeO<sub>4</sub> nanorods, see Fig. 10b, in order to improve the photocatalytic activity of Zn<sub>2</sub>GeO<sub>4</sub> for CO<sub>2</sub> reduction [231]. The resultant nanocomposite has both high crystallinity and CO<sub>2</sub> adsorption capacity due to Zn<sub>2</sub>GeO<sub>4</sub> and ZIF-8 respectively, thus displaying 62% enhancement in CO<sub>2</sub> reduction than Zn<sub>2</sub>GeO<sub>4</sub> nanorods. This optimum conversion is achieved when the composite material contains 25 wt% ZIF-8 with a higher CO<sub>2</sub> adsorption capacity (3.8 times) than the Zn<sub>2</sub>GeO<sub>4</sub> nanorods. While Zn<sub>2</sub>GeO<sub>4</sub> nanorods can

produce 1.43  $\mu\text{mol g}^{-1}$  of the liquid fuel ( $\text{CH}_3\text{OH}$ ), the composite can generate 2.44  $\mu\text{mol g}^{-1}$  [231].

By photoelectrochemical impedance and PL measurements, it has been revealed that uniform ultrathin 2D Zn porphyrin-based MOF nanosheets (4.7 nm thickness) as a photosensitizer have a higher charge transport mobility and better suppression of charge recombination than the Zn-MOF bulk [232]. Thus, Zn-MOF nanosheets higher activity (68.7 TONs of CO) and selectivity (81.5%) than the Zn-MOF bulk (26.2 TONs of CO and 67.9% selectivity). In addition, with ZIF-8 as co-catalyst, the Zn-MOF nanosheets can generate up to 117.8 TON and 91.0% selectivity, while 63.6 TON and 89.5% selectivity could be realized for the bulk [232].

A composite consisting of porphyrin-based MOFs, Al/PMOF, and amine functionalized graphene,  $\text{NH}_2\text{-rGO}$ , was

evaluated for the photocatalytic  $\text{CO}_2$  reduction [233].  $\text{NH}_2\text{-rGO}$  (5 wt%)/Al-PMOF recorded a formate production rate of 685.6  $\mu\text{mol/g}_{\text{cat}}^{-1}\text{h}^{-1}$  with high selectivity (almost 100%). The catalytic activity of the graphene-porphyrin based MOF outperformed that of Al-PMOF and porphyrin ligand.

A semiconductive Cu(I)/Cu(II) mixed-valence MOF, NJU-Bia61 (NJU-Bai for Nanjing University Bai group) with the full light spectrum, containing  $\text{Cu}_4\text{I}_4$  and  $\text{Cu}_3\text{OI}(\text{CO}_2)_3$  clusters, exhibited  $\text{CO}_2$  adsorption capacity of 29.82  $\text{cm}^3 \text{g}^{-1}$  and photocatalytic  $\text{CO}_2$  reduction to produce  $\text{CH}_4$  at a rate of 15.75  $\text{mmol g}^{-1} \text{h}^{-1}$  and with high selectivity (72.8%) [234]. These unique metal clusters play the role of photoelectron generators and collectors. **Table 3** presents MOFs/semiconductor composites that have been utilized for photocatalytic  $\text{CO}_2$  reduction.

**Table 3** MOFs/semiconductor hybrid photocatalysts

Acronym/Empirical formula	Semiconductor	Catalytic Active Site	Product amount/Time	Ref
Co-ZIF-9	$[\text{Ru}(\text{bpy})_3]\text{Cl}_2 \cdot 6\text{H}_2\text{O}$	Cobalt-cluster	450 TON of CO within 2.5 hours	[209]
Co-ZIF-9	$\text{g-C}_3\text{N}_4$	Co-ZIF-9 Cobalt-cluster	20.8 $\mu\text{mol}$ CO in 2 h	[230]
Co-ZIF-9	CdS	Co-ZIF-9	85.6 $\mu\text{mol}$ CO in 3 h	[210]
ZIF-8	$\text{Zn}_2\text{GeO}_4$	ZIF-8	2.44 $\mu\text{mol g}^{-1}$ $\text{CH}_3\text{OH}$ in 11 h	[231]

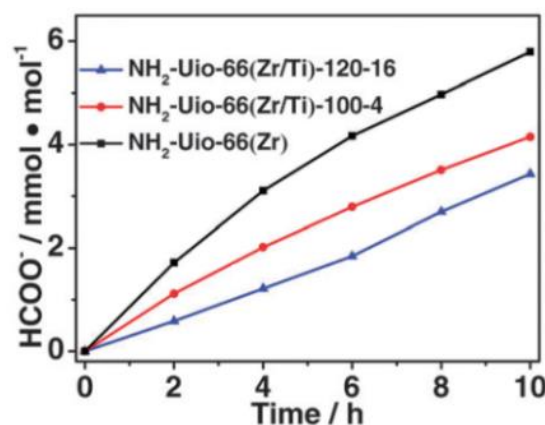


Cu <sub>3</sub> (BTC) <sub>2</sub> (HKUST-1)	TiO <sub>2</sub>	Cu sites of Cu 3(BTC) <sub>2</sub>	2.65 μmol g <sup>-1</sup> CH <sub>4</sub>	[217]
MIL-101- NH <sub>2</sub> (Al)	[Ru(bpy)2(4,4'- bpydc)] <sup>2+</sup>	[Cp*Rh(4,4'- bpydc)] <sup>2+</sup>	0.33 μmol HCOO <sup>-</sup> in 5 h	[186]

### 4.3. Double metal node by doping

Through the concept of metal ions metathesis [235], post-synthetic metal exchange (PSE) has been introduced as a facile strategy for tuning of the metal nodes of MOFs [236, 237] to achieve enhanced photocatalytic CO<sub>2</sub> reduction [238]. Li and coworkers [208] prepared a Ti-substituted NH<sub>2</sub>-UiO-66(Zr) (NH<sub>2</sub>-UiO-66(Zr/Ti)) by PSE of Zr with Ti, thereby generating oxo-bridged Ti<sup>4+</sup>-O-Zr<sup>4+</sup> bimetallic assemblies within the same frameworks. Such oxo-bridged bimetallic assemblies in the SBU of NH<sub>2</sub>-UiO-66(Zr/Ti) represented as (Ti<sup>4+/Zr<sup>4+</sup></sup>)<sub>6</sub>O<sub>4</sub>(OH)<sub>4</sub> are similar to those previously constructed over semiconductors and zeolites, like; Zr<sup>4+</sup>-O-Cu<sup>+</sup>, Ti<sup>4+</sup>-O-Fe<sup>2+</sup>, Cu<sup>+</sup>-O-Zr<sup>4+</sup> and (Ti<sup>4+</sup>-O-Cr<sup>3+</sup>, Ti<sup>4+</sup>-O-Co<sup>2+</sup> and Ti<sup>4+</sup>-O-Ce<sup>3+</sup>) [239-241]. In addition, oxo-bridged hetero-metallic assemblies formed by partial substitution of transition metal cations have been reported in MOFs [242-244]. Li and coworkers used DFT calculations and ESR analysis results to confirm that the incorporated Ti substituent acts as a mediator, thereby facilitating electron

transfer from the activated linker to the Zr<sup>4+</sup> reactive site, enhancing the catalytic performance [208]. As illustrated in Fig. 11, the sample synthesized at 120 °C for 16 days denoted as NH<sub>2</sub>-UiO-66(Zr/Ti)-120-16 contains 53.4 % Ti and generated 5.8 mmol mol<sup>-1</sup> of formate after 10 h irradiation, thus outperforming (1.7 times higher) NH<sub>2</sub>-UiO-66(Zr). In addition, Cohen and coworkers used a dual (Zr/Ti) node framework obtained by PSE of Ti(IV) into a mixed linker Zr-based MOF to lower the electron-accepting level of the SBUs, thereby improving the CO<sub>2</sub> reduction to formate under visible light irradiation [172].



**Fig. 11.** Photocatalytic performance of single and bimetallic amine-based MOFs.

Reproduced with permission [178]. Copyright 2015, The Royal Society of Chemistry.

## 5. Enhancing the CO<sub>2</sub> adsorption of MOF photocatalysts

Generally, a photocatalyst that has more adsorption capability toward CO<sub>2</sub> stands a better chance of enhanced CO<sub>2</sub> reduction activity. Therefore, some modification strategies have been devised to improve the CO<sub>2</sub> adsorption of MOF-based photocatalysts in order to achieve higher performance.

### 5.1. Organic-linker modification

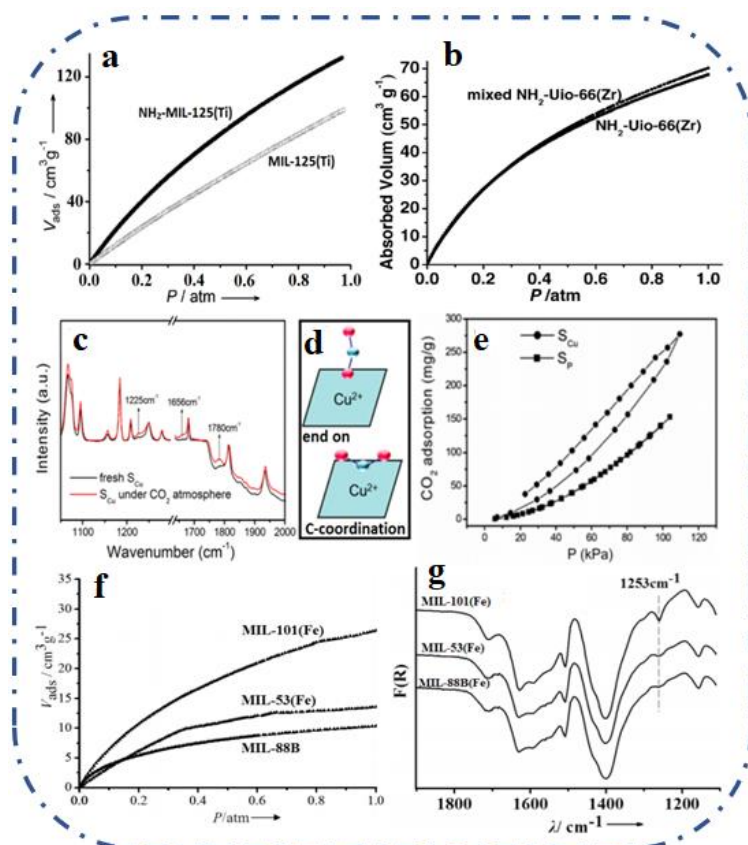
The CO<sub>2</sub> intermolecular interaction with aromatic molecules can be augmented by functionalization of the aromatic ring with some polar substituents like -NH<sub>2</sub>, -OH or -SO<sub>3</sub>H, or -COOH, thereby enhancing the adsorption capacity [245, 246]. Torrisi et al. used DFT computation to show that the strongest interaction is experienced with lone pair donating atoms (N, O) followed by the acidic protons of SO<sub>3</sub>H and COOH, and the least with hydrogen-bond-like interactions with aromatic H [245]. By comparing the CO<sub>2</sub> adsorption capacity of NH<sub>2</sub>-MIL-125(Ti) is higher (132.2 cm<sup>3</sup>g<sup>-1</sup>) than that of MIL-125(Ti) (98.6 cm<sup>3</sup>g<sup>-1</sup>), Fig. 12a [71].

In addition, an increase in the amino functionality in a linker enhances the CO<sub>2</sub> adsorption. By using mixed linker, H<sub>2</sub>ATA and 2,5-diaminoterephthalic acid (H<sub>2</sub>DTA), for MOFs synthesis, about 4% higher CO<sub>2</sub> adsorption was obtained when compared with that prepared with only H<sub>2</sub>ATA (Fig. 12b) [80]. Xing and co-workers illustrated that increasing the ligand length and the amount of amine group synergistically improve the CO<sub>2</sub> adsorption capacity of MOF-based catalyst [247]. Comparatively, Zr-SDCA-NH<sub>2</sub> has up to 23% enhancement in CO<sub>2</sub> adsorption than that of NH<sub>2</sub>-UiO-66(Zr) [80].

### 5.2 Metal-nodes engineering

Chemisorption of CO<sub>2</sub> is a beneficial strategy to enhance its adsorption [187]. In-situ FT-IR analysis showed that chemisorption of CO<sub>2</sub> on porphyrin-based MOF containing Cu<sup>2+</sup> results in a higher amount of CO<sub>2</sub> adsorption capacity 277.4 mg/g than the physisorption of its analogue (without Cu<sup>2+</sup>) 153.1 mg/g (Fig. 12c). The chemisorption occurred at the Cu site by the “end-on” or “C-coordination” mode, as shown in Fig. 12d. In addition, the open adsorption–desorption isotherm (Fig. 12e) of the Cu<sup>2+</sup> tethered MOFs indicates chemical adsorption.





**Fig. 12.** (a) CO<sub>2</sub> adsorption isotherms of MIL-125(Ti) and NH<sub>2</sub>-MIL-125(Ti), Reproduced with permission [69]. Copyright 2012, Wiley-VCH and (b) mixed ligand with enhanced adsorption of CO<sub>2</sub>. Reproduced with permission [78]. Copyright 2013, Wiley-VCH. (c) In situ FT-IR spectra of SCu under different atmosphere, (d) The adsorption geometry “end-on” and “C-coordination” of CO<sub>2</sub> on SCu, (e) adsorption-desorption isotherm of the Cu<sup>2+</sup> tethered MOFs. Adapted with permission [160]. Copyright 2013, American Chemical Society. (f) CO<sub>2</sub> adsorption isotherms and (g) in-situ FT-IR analyses of MIL-88(Fe), MIL-53(Fe) and MIL-101(Fe). Reproduced with permission [70]. Copyright 2014, American Chemical Society.

By examining the CO<sub>2</sub> adsorption capacity of different Fe-based MOFs, it has been proven that the occurrence of coordination unsaturated metal sites (CUSs) enhances the adsorption potential. As shown in Fig. 12f, the presence of unsaturated Fe sites in MIL-101(Fe) enhanced

its CO<sub>2</sub> adsorption capacity (26.4 g/cm<sup>3</sup>), which is higher than the values, 10.4 and 13.5 g/cm<sup>3</sup>, recorded for MIL-88B(Fe) and MIL-53(Fe) respectively [72]. When CO<sub>2</sub> was injected in MIL-101(Fe), a new peak (1253 cm<sup>-1</sup>) emerged in the *in-situ* FT-IR spectrum, see Fig. 12g. This new peak is attributed to the

bidentate carbonate bonded to the metal center [248]. Consequently, confirming that there is direct adsorption of carbon dioxide onto the Fe cluster because of the existence of CUSs in MIL-101(Fe) [72, 249]. Conversely, no peaks were observed between 1250 and 1270  $\text{cm}^{-1}$ , for both MIL-88B(Fe) and MIL-53(Fe), proving the absence of CUSs in both frameworks. In addition, the synergistic corporation between MOFs with open alkaline metal sites enhances  $\text{CO}_2$  photoreduction. CPO-27-Mg/ $\text{TiO}_2$  nanocomposite with intimate contact between  $\text{TiO}_2$  nanospheres and spindle-shaped CPO-27-Mg microcrystal exhibited improved catalytic activity for the conversion of  $\text{CO}_2$  into CO and  $\text{CH}_4$  in the presence of light [141]. The enhanced performance was due to the presence of open alkaline metal sites  $\text{Mg}^{2+}$  (beneficial for  $\text{CO}_2$  activation) that resulted in high  $\text{CO}_2$  adsorption capacity.

Improvement in  $\text{CO}_2$  adsorption of MOFs photocatalyst can be achieved by incorporating double metal nodes in the SBU of the framework. The two MOFs containing (Zr/Ti) nodes show around  $83 \text{ cm}^3 \text{ g}^{-1}$   $\text{CO}_2$  adsorption capacity, which is higher than the value ( $68 \text{ cm}^3 \text{ g}^{-1}$ ) recorded for the framework with single metal node [208]. Similarly, Lau et al. showed that PSE of  $\text{Ti}^{4+}$  into Zirconium MOF doubled their  $\text{CO}_2$  adsorption capacity, attributed to

smaller pore size (enhances  $\text{CO}_2$  isosteric heat) and higher adsorption enthalpy [250].

### 5.3 Morphology Control

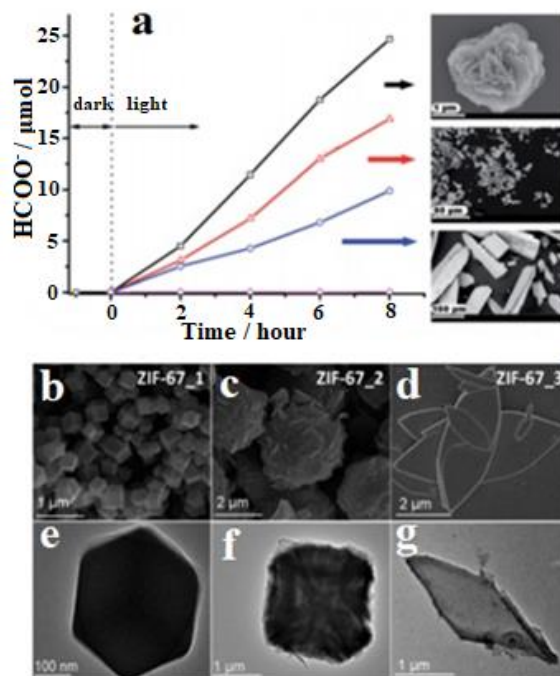
MOF-photocatalysts are amenable to fine-tuning through morphology and size control [251], which are among the strategies to enhance the photocatalytic performance of MOFs for  $\text{CO}_2$  reduction. For example, MOFs with an increased surface area have a higher  $\text{CO}_2$  adsorption capacity resulting in improved photoreduction activities. By bifunctional Ru-MOF, Shuquan et al. designed 3D metal-organic flower-like hierarchical nanostructures to evaluate the effect of morphology on activity [252]. The unique flower-like nanostructure of the Ru-polypyridine-based MOFs impacts higher surface area with shorter energy transfer path length, thereby improving their visible-light photocatalytic  $\text{CO}_2$  reduction activity to almost 150 % more than micro-lamellate MOFs, Fig. 13a. Furthermore, the flower-like structure promotes the recyclability and photostability of the MOFs catalyst.

In a similar development, the catalytic performance of ZIF-67, with different morphologies, was evaluated using  $[\text{Ru}(\text{bpy})_3]^{2+}$  as the photosensitizer [253]. It was established that the leaf-like 2D laminated ZIF-67\_3, see Fig. 13d, displayed the best  $\text{CO}_2$  photoreduction performance and the highest

stability compared with the rhombic dodecahedral morphology framework. The best activity was attributed to their highest CO<sub>2</sub> uptake capacity and efficient transfer of electrons from [Ru(bpy)<sub>3</sub>]<sup>2+</sup> to the leaf-like ZIF-67 structure.

In another work, Sun and co-workers explored the structure-dependent photocatalytic CO<sub>2</sub> conversion performance by comparing the activities of two Fe-based MOFs, MIL-100(Fe) and MIL-101(Fe) [254]. Under visible-light irradiation, MIL-100(Fe) exhibited higher catalytic activity and selectivity for CO<sub>2</sub>-to-CH<sub>4</sub> conversion. Although both frameworks contain the same four μ<sub>3</sub>-O-bridged Fe<sub>3</sub>O clusters, however, the MIL-100(Fe) structural unit is more closely arranged than the one of MIL-101(Fe) and the Fe<sub>3</sub>O clusters density of MIL-100(Fe) is higher. Hence, the structure of MIL-100(Fe) is more conducive for electron transfer. These attributed to the higher performance and selectivity of MIL-100(Fe).

Niu et al. showed a photochemical method for the preparation of a *spongy* nickel-organic hybrid structure, Ni(TPA/TEG), with high amount of defects, which is efficient for CO<sub>2</sub> reduction having a highly selective remarkable production of CO (a rate of 15,866 mmol hour<sup>-1</sup> g<sup>-1</sup>) [157]. The catalyst gives near 100%



**Fig. 13.** (a) The CO<sub>2</sub> photoreduction over Ru-MOF (blue), microcrystals (red), nanoflowers (black) and without a sample (pink). Reproduced with permission [220]. Copyright 2015, The Royal Society of Chemistry. SEM images of different morphologies of ZIF-67, (b), (c) and (d) (first row) the corresponding TEM images of the samples (e), (f), and (g) (second row). Reproduced with permission [221]. Copyright 2018, The Royal Society of Chemistry.

CO selectivity over other competing gases like H<sub>2</sub> or CH<sub>4</sub>.

Zhang et al. employed structural interpenetration to improve the stability of Ru-polypyridine-based MOFs [189]. They rationally designed 2-fold interpenetrated and non-interpenetrated Ru-MOFs with similar

CO<sub>2</sub> photoreduction activity within the initial 6 hours. The interpenetrated frameworks' activity continued up to 12 hours (30 μmol formate generated) but could not be sustained for its counterpart. It was established that the interwoven framework has good durability and recyclability, thus showing higher photonic and thermal stability than their non-interpenetrated counterpart. The remarkable stability results from the numerous interframework supramolecular interactions [189].

## 6. Conclusions and future perspectives

High-performance CO<sub>2</sub> reduction MOF photocatalysts are achievable by following the three fundamental strategies: engineering the light-harvesting components of frameworks, improving their charge dynamics performance, and enhancing the CO<sub>2</sub> adsorption performance of the MOFs. Bandgap engineering, by incorporating visible light-responsive conjugates and functionalities into the MOFs backbone, is an established strategy of increasing the optical efficiency of the MOFs. Incorporation of appropriate visible light-responsive linkers and redox-active metal in a particular MOF, i.e., double excitation mechanism, enhance the overall light absorption capacity of the frameworks. Synthetically, the proximal combination of active metalloligands and light-responsive

ligand coupled with immobilization of an appropriate amount of photosynthesizer enhances the photonic and quantum efficiency. The limitation of MOF photocatalyst, having modest/insufficient thermal and chemical stability, resulted that most reported MOFs for CO<sub>2</sub> reduction are constructed with high-valent metals ions containing intense charge density, such as Zr<sup>4+</sup>, Al<sup>3+</sup>, and Cr<sup>3+</sup>, forming MOFs with strong coordination bonds. Since artificial photosynthesis and MOF photocatalysts are unavoidably handled in air containing moisture, water stability is very crucial and fundamental while analyzing the stability of the frameworks. Composite material engineering and structural processing via post-synthetic modifications have been used to augment the stability of already prepared MOF materials. For charge balance, these high-valent metal ions warrant more linkers, thereby resulting in a high connection number in the metal nodes and high stability of the resultant MOF photocatalysts. In addition, these high-valent ion-based frameworks have a significant level of acid stability. Notwithstanding that these robust SBU can withstand harsh photocatalytic conditions, they lack photo- and redox-activities, hence limiting their CO<sub>2</sub> reduction proficiency. Designing SBU with efficient electron transfer containing a high density of unsaturated metal ions and at the

same time incorporating bimetallic nodes in which one or both metal ions will be visible light-responsive significantly improves the efficiency and stability of the MOF photocatalysts. Like, using oxo-bridged bimetallic assemblies of  $Ti^{4+}-O-Fe^{2+}$  or  $Ti^{4+}-O-Co^{2+}$ , with unsaturated Fe or Co ions which are active redox metals, will not only increase the  $CO_2$  adsorption capacity but also improve both the visible light absorption and the overall  $CO_2$  reduction activity. Higher charge carrier mobility is realizable by noble metal or metal nanoparticle loading, thus generating plasmonic effect and/or redox matching between the SBU and the linker. Using electron-rich metal nodes or organic ligands also improves charge mobility.

The relatively weak  $CO_2$ -framework interactions at low partial pressure limit the application of light-responsive MOFs to convert  $CO_2$  to solar fuels. This shortfall can be overcome/improved by incorporating  $CO_2$ -philic moieties on the framework's linker. Therefore, functionalizing the linker with amine, porphyrin, imidazole, and other  $CO_2$ -philic containing moieties have proven efficient in improving the carbon dioxide adsorption performance of the MOFs. Moreover, metal-node engineering by chemisorption of  $CO_2$  and morphology control during synthesis are other confirmed strategies

to enhance the  $CO_2$  adsorptive features of MOF photocatalysts. It is further beneficial that most of these  $CO_2$ -philic linkers are even light-responsive. Critically having discussed the underlying principles to enhance the performance of  $CO_2$  photofixation into solar fuels using MOF photocatalyst, this review can trigger intensive, innovative study in this area and open new research doorways for the design of efficient complex multicomponent photosystems that can achieve artificial photosynthesis.

### Abbreviations

- 1) Ti-MCM-41 and Ti-MCM-48 = Titanium-mobil composite of matter No. 41 and No. 48
- 2)  $pd^{2-}$  = pyrazine-2,3-dithiolate
- 3)  $H_3btc$  = 1,3,5-benzenetricarboxylic acid
- 4) HITP=2,3,6,7,10,11-hexaiminotriphenylene
- 5)  $[Zr_6O_4(OH)_4(L)_6] \cdot 8DMF$ ;  $H_2L$  = 2,2'-diamino-4,4'-stilbenedicarboxylic acid, DMF = Dimethylformamide
- 6)  $H_2TCPP$  = tetrakis(4-carboxyphenyl)-porphyrin
- 7)  $H_2L_4$  =  $Re(CO)_3(dcbpy)Cl$ ,  $bpdc$  = 5,5'-biphenyldicarboxylate, MOF-4 =  $Zr_6(\mu_3-O)_4(\mu_3-OH)_4(bpdc)_{5.83}(L_4)_{0.17}$
- 8)  $bpy$  = 2,2'-bipyridine
- 9)  $bpydc$  = bipyridinedicarboxylic acid
- 10)  $dmb$  = 4,4'-dimethyl-2,2'-bipyridine
- 11) BNAH = 1-benzyl-1,4-dihydronicotinamide
- 12)  $Cp^*$  = pentamethylcyclopentadienyl
- 13)  $DMBD$  = 2,5-dimercapto-1,4-benzenedicarboxylate

- 14) TEOA = triethanolamine
- 15)  $[\text{Co}_2(\text{HAD})_2(\text{AD})_2(\text{BA})] \cdot \text{DMF} \cdot 2\text{H}_2\text{O}$  (ADMOF-1; HAD = adenine and BA = butanedioic acid)
- 16)  $[\text{Co}_2(\text{HAD})_2(\text{AD})_2(\text{IA})_2] \cdot \text{DMF}$  (AD-MOF-2; IA = isobutyric acid)
- 17)  $\text{H}_2\text{SDCA-NH}_2$  = 2,2'-diamino-4,4'-stilbenedicarboxylic acid
- 18) Rh-PMOF-1 = rhodium(III)-porphyrin-based MOF
- 19) TCPP=4,4',4'',4'''-(porphyrin-5,10,15,20-tetrayl) tetrabenzoate
- 20) CCNS = carbon nitride nanosheets
- 21) HKUST-1 = Hong Kong University of Science and Technology-1
- 22) IPCE = incident-photon-to-current conversion efficiency
- 23) ZIF = zeolitic imidazolate framework
- 24) Cyclam = 1,4,8,11-tetraazacyclotetradecane
- 25) LHP = lead halide perovskite
- 26) QDs = quantum dots
- 27) g- $\text{C}_3\text{N}_4$  = graphitic carbon nitride
- 28) PSE = post-synthetic metal exchange
- 29) DOBDC = 2,5-dioxido-1,4-benzenedicarboxylate
- 30) SBUs = secondary building units

### Acknowledgements

C.I.E. and F.V. gratefully acknowledge Wuhan University of Technology for financial support. S.L. acknowledge the financial support of the National Natural Science Foundation of China (51572209 and 51872341), the Fundamental Research Funds for the Central Universities (19lgzd29), the Tip-top Scientific and Technical Innovative Youth Talents of Guangdong Special

Support Program (2019TQ05L196) and the Science and Technology Planning Project of Guangdong Province (2020A0505100033 and 2021A1515010147). C.I.E. acknowledge European Union's Horizon 2020 research and innovation programme under the Marie Skłodowska-Curie grant agreement No 754382.

### References

- [1] C.D. Windle, R.N. Perutz, *Coord. Chem. Rev.* 256 (2012) 2562-2570.
- [2] R. Kiesgen de\_Richter, T. Ming, S. Caillol, *Renewable Sustainable Energy Rev.* 19 (2013) 82-106.
- [3] S.C. Roy, O.K. Varghese, M. Paulose, C.A. Grimes, *Acs Nano* 4 (2010) 1259-1278.
- [4] J.-R. Li, Y. Ma, M.C. McCarthy, J. Sculley, J. Yu, H.-K. Jeong, P.B. Balbuena, H.-C. Zhou, *Coord. Chem. Rev.* 255 (2011) 1791-1823.
- [5] M. Khalil, J. Gunlazuardi, T.A. Ivandini, A. Umar, *Renewable Sustainable Energy Rev.* 113 (2019) 109246.
- [6] C. Bie, B. Cheng, J. Fan, W. Ho, J. Yu, *EnergyChem* 3 (2021) 100051.
- [7] G.A. Olah, A. Goeppert, G.S. Prakash, 74 (2008) 487-498.
- [8] K.M.K. Yu, I. Curcic, J. Gabriel, S.C.E. Tsang, *ChemSusChem* 1 (2008) 893-899.
- [9] H. Takeda, O. Ishitani, *Coord. Chem. Rev.* 254 (2010) 346-354.
- [10] O. Ellabban, H. Abu-Rub, F. Blaabjerg, *Renewable Sustainable Energy Rev.* 39 (2014) 748-764.
- [11] I. Shown, S. Samireddi, Y.-C. Chang, R. Putikam, P.-H. Chang, A. Sabbah, F.-Y. Fu, W.-F. Chen, C.-I. Wu, T.-Y. Yu, *Nat. Commun.* 9 (2018) 169.
- [12] G.D. Scholes, G.R. Fleming, A. Olaya-Castro, R. Van Grondelle, *Nat. Chem.* 3 (2011) 763.
- [13] M.A. Asraf, C.I. Ezugwu, C.M. Zakaria, F. Verpoort, *Photochem. Photobiol. Sci.* 18 (2019) 2782-2791.
- [14] T. Zhang, W. Lin, *Chem. Soc. Rev.*, 43 (2014) 5982-5993.

- [15] S. Zhang, H. Ye, J. Hua, H. Tian, *EnergyChem* 1 (2019) 100015.
- [16] E. Kabir, P. Kumar, S. Kumar, A.A. Adelodun, K.-H. Kim, *Renewable Sustainable Energy Rev.* 82 (2018) 894-900.
- [17] K.E. Dalle, J. Warnan, J.J. Leung, B. Reuillard, I.S. Karmel, E. Reisner, *Chem. Rev.* 119 (2019) 2752-2875.
- [18] L. Hammarstrom, S. Hammes-Schiffer, *Acc. Chem. Res.* 42 (2009) 1859-1860.
- [19] J. Gong, C. Li, M.R. Wasielewski, *Chem. Soc. Rev.* 48 (2019) 1862-1864.
- [20] X. Chang, T. Wang, J. Gong, *Energy Environ. Sci.* 9 (2016) 2177-2196.
- [21] C. Chen, Y. Chen, R. Yao, Y. Li, C. Zhang, *Angew. Chem.* 131 (2019) 3979-3982.
- [22] O. Kruse, J. Rupprecht, J.H. Mussnug, G.C. Dismukes, B. Hankamer, *Photochem. Photobiol. Sci.* 4 (2005) 957-970.
- [23] R.J. Cogdell, A.T. Gardiner, N. Yukihiro, H. Hashimoto, *J. Photochem. Photobiol. A* 353 (2018) 645-653.
- [24] D. Kim, K.K. Sakimoto, D. Hong, P. Yang, *Angew. Chem. Int. Ed.* 54 (2015) 3259-3266.
- [25] M. Schreier, L. Curvat, F. Giordano, L. Steier, A. Abate, S.M. Zakeeruddin, J. Luo, M.T. Mayer, M. Grätzel, *Nat. Commun.* 6 (2015) 7326.
- [26] S.N. Villadsen, P.L. Fosbøl, I. Angelidaki, J.M. Woodley, L.P. Nielsen, P. Møller, *ChemSusChem* 12 (2019) 2147-2153.
- [27] M.S. Akple, J. Low, S. Liu, B. Cheng, J. Yu, W. Ho, *J. CO<sub>2</sub> Util.* 16 (2016) 442-449.
- [28] H. Yang, Z. Xu, M. Fan, R. Gupta, R.B. Slimane, A.E. Bland, I. Wright, *J. Environ. Sci.* 20 (2008) 14-27.
- [29] M. Ghoussoub, M. Xia, P.N. Duchesne, D. Segal, G. Ozin, *Energy Environ. Sci.* 12 (2019) 1122-1142.
- [30] M.M. Flores-Granobles, M. Saeys, *Energy Environ. Sci.* 13 (2020) 1923-1932.
- [31] S. Liu, F. Chen, S. Li, X. Peng, Y. Xiong, *Appl. Catal. B* 211 (2017) 1-10.
- [32] J. Low, J. Yu, W. Ho, *J. Phys. Chem. Lett.* 6 (2015) 4244-4251.
- [33] C.-Y. Lee, J. Zou, J. Bullock, G.G. Wallace, *J. Photochem. Photobiol. C* 39 (2019) 142-160.
- [34] G. Centi, E.A. Quadrelli, S. Perathoner, *Energy Environ. Sci.* 6 (2013) 1711-1731.
- [35] A. Fujishima, *Nature* 238 (1972) 37-38.
- [36] M.S. Akple, J. Low, Z. Qin, S. Wageh, A.A. Al-Ghamdi, J. Yu, S. Liu, *Chin. J. Catal.* 36 (2015) 2127-2134.
- [37] S. Liu, J. Xia, J. Yu, *ACS Appl. Mater. Interfaces* 7 (2015) 8166-8175.
- [38] Y. He, Y. Wang, L. Zhang, B. Teng, M. Fan, *Appl. Catal. B* 168 (2015) 1-8.
- [39] H.-Y. Wu, H. Bai, J.C. Wu, *Ind. Eng. Chem.* 53 (2014) 11221-11227.
- [40] M. Anpo, H. Yamashita, K. Ikeue, Y. Fujii, S.G. Zhang, Y. Ichihashi, D.R. Park, Y. Suzuki, K. Koyano, T. Tatsumi, *Catal. Today* 44 (1998) 327-332.
- [41] X. Liu, M. Ye, S. Zhang, G. Huang, C. Li, J. Yu, P.K. Wong, S. Liu, *J. Mater. Chem. A* 6 (2018) 24245-24255.
- [42] Q. Xie, W. He, S. Liu, C. Li, J. Zhang, P.K. Wong, *Chin. J. Catal.* 41 (2020) 140-153.
- [43] E.D.A. Mário, C. Liu, C.I. Ezugwu, S. Mao, F. Jia, S. Song, *Appl. Clay Sci.* 184 (2020) 105370.
- [44] K. Sumida, D.L. Rogow, J.A. Mason, T.M. McDonald, E.D. Bloch, Z.R. Herm, T.-H. Bae, J.R. Long, *Chem. Rev.* 112 (2011) 724-781.
- [45] R. Vaidhyanathan, S.S. Iremonger, G.K. Shimizu, P.G. Boyd, S. Alavi, T.K. Woo, *Science* 330 (2010) 650-653.
- [46] N. Ahmad, A.H. Chughtai, H.A. Younus, F. Verpoort, *Coord. Chem. Rev.* 280 (2014) 1-27.
- [47] S. Kitagawa, R. Kitaura, S.i. Noro, *Angew. Chem. Int. Ed.* 43 (2004) 2334-2375.
- [48] J.L. Rowsell, O.M. Yaghi, *Microporous Mesoporous Mater.* 73 (2004) 3-14.
- [49] A.U. Czaja, N. Trukhan, U. Müller, *Chem. Soc. Rev.* 38 (2009) 1284-1293.
- [50] S.R. Batten, N.R. Champness, X.-M. Chen, J. Garcia-Martinez, S. Kitagawa, L. Öhrström, M. O'Keeffe, M.P. Suh, J. Reedijk, *Pure Appl. Chem.* 85 (2013) 1715-1724.
- [51] C.I. Ezugwu, N.A. Kabir, M. Yusubov, F. Verpoort, *Coord. Chem. Rev.* 307 (2016) 188-210.
- [52] O.K. Farha, I. Eryazici, N.C. Jeong, B.G. Hauser, C.E. Wilmer, A.A. Sarjeant, R.Q. Snurr, S.T. Nguyen, A.O. Yazaydin, J.T. Hupp, *J. Am. Chem. Soc.* 134 (2012) 15016-15021.
- [53] H. Furukawa, N. Ko, Y.B. Go, N. Aratani, S.B. Choi, E. Choi, A.Ö. Yazaydin, R.Q.



- Snurr, M. O’Keeffe, J. Kim, *Science* 329 (2010) 424-428.
- [54] C.I. Ezugwu, S. Zhang, S. Li, S. Shi, C. Li, F. Verpoort, J. Yu, S. Liu, *Environ. Sci. Nano* 6 (2019) 2931-2936.
- [55] S.E. Henkelis, D.L. Huber, D.J. Vogel, J.M. Rimsza, T.M. Nenoff, *ACS Appl. Mater. Interfaces* 12 (2020) 19504-19510.
- [56] C. Orellana-Tavra, E.F. Baxter, T. Tian, T.D. Bennett, N.K. Slater, A.K. Cheetham, D. Fairen-Jimenez, *Chem. Commun.* 51 (2015) 13878-13881.
- [57] A.R. Chowdhuri, D. Bhattacharya, S.K. Sahu, *Dalton Trans.* 45 (2016) 2963-2973.
- [58] L.E. Kreno, K. Leong, O.K. Farha, M. Allendorf, R.P. Van Duyne, J.T. Hupp, *Chem. Rev.* 112 (2011) 1105-1125.
- [59] A.J.M. Reddy, N. Katari, P. Nagaraju, S.M. Surya, *Mater. Chem. Phys.* 241 (2020) 122357.
- [60] C.I. Ezugwu, M.A. Asraf, X. Li, S. Liu, C.-M. Kao, S. Zhuiykov, F. Verpoort, *J. Colloid Interface Sci.* 519 (2018) 214-223.
- [61] C.I. Ezugwu, M.A. Asraf, X. Li, S. Liu, C.-M. Kao, S. Zhuiykov, F. Verpoort, *Data Brief* 18 (2018) 1952-1961.
- [62] M. Eddaoudi, D.F. Sava, J.F. Eubank, K. Adil, V. Guillermin, *Chem. Soc. Rev.* 44 (2015) 228-249.
- [63] A.H. Chughtai, N. Ahmad, H.A. Younus, A. Laypkov, F. Verpoort, *Chem. Soc. Rev.* 44 (2015) 6804-6849.
- [64] B. Mousavi, S. Chaemchuen, C.I. Ezugwu, Y. Yuan, F. Verpoort, *Appl. Organomet. Chem.* 32 (2018) e4062.
- [65] C.I. Ezugwu, B. Mousavi, M.A. Asrafa, A. Mehta, H. Vardhan, F. Verpoort, *Catal. Sci. Technol.* 6 (2016) 2050-2054.
- [66] A. Zanon, S. Chaemchuen, B. Mousavi, F. Verpoort, *J. CO<sub>2</sub> Util.* 20 (2017) 282-291.
- [67] X. Li, S. Liu, K. Fan, Z. Liu, B. Song, J. Yu, *Adv. Energy Mater.* 8 (2018) 1800101.
- [68] H. Li, M. Eddaoudi, M. O’Keeffe, O.M. Yaghi, *Nature* 402 (1999) 276-279.
- [69] S.L. James, *Chem. Soc. Rev.* 32 (2003) 276-288.
- [70] N. Heidary, T.G. Harris, K.H. Ly, N. Kornienko, *Physiol. Plant* 166 (2019) 460-471.
- [71] Y. Fu, D. Sun, Y. Chen, R. Huang, Z. Ding, X. Fu, Z. Li, *Angew. Chem.* 124 (2012) 3420-3423.
- [72] D. Wang, R. Huang, W. Liu, D. Sun, Z. Li, *ACS Catal.* 4 (2014) 4254-4260.
- [73] G. Zhou, M.-F. Wu, Q.-J. Xing, F. Li, H. Liu, X.-B. Luo, J.-P. Zou, J.-M. Luo, A.-Q. Zhang, *Appl. Catal. B* 220 (2018) 607-614.
- [74] D. Sun, S. Jang, S.J. Yim, L. Ye, D.P. Kim, *Adv. Funct. Mater.* 28 (2018) 1707110.
- [75] F. Leng, H. Liu, M. Ding, Q.-P. Lin, H.-L. Jiang, *ACS Catal.* 8 (2018) 4583-4590.
- [76] S. Liu, J. Wang, J. Yu, *RSC Adv.* 6 (2016) 59998-60006.
- [77] C. Bozal-Ginesta, J. Durrant, *Faraday Discuss.* 215 (2019) 439-451.
- [78] W.-J. Ong, L.-L. Tan, Y.H. Ng, S.-T. Yong, S.-P. Chai, *Chem. Rev.* 116 (2016) 7159-7329.
- [79] C. I. Ezugwu, O. T. Ujam, P. O. Ukoha, N. N. Ukwueze, *Chem. Sci. Trans.* 2 (2013) 1118-1125.
- [80] D. Sun, Y. Fu, W. Liu, L. Ye, D. Wang, L. Yang, X. Fu, Z. Li, *Chem. Eur. J.* 19 (2013) 14279-14285.
- [81] S.-L. Li, Q. Xu, *Energy Environ. Sci.* 6 (2013) 1656-1683.
- [82] C.-C. Wang, J.-R. Li, X.-L. Lv, Y.-Q. Zhang, G. Guo, *Energy Environ. Sci.* 7 (2014) 2831-2867.
- [83] G. Liu, Y. Sheng, J.W. Ager, M. Kraft, R. Xu *EnergyChem* 1 (2019) 100014.
- [84] A. Corma, H. Garcia, *Chem. Commun.* (2004) 1443-1459.
- [85] C.-C. Hou, H.-F. Wang, C. Li, Q. Xu, *Energy Environ. Sci.* 7 (2014) 2831-2867.
- [86] A. Yan, X. Shi, F. Huang, M. Fujitsuka, T. Majima, *Appl. Catal. B* 250 (2019) 163-170.
- [87] K. Wang, Y. Li, J. Li, G. Zhang, *Appl. Catal. B* (2019) 117730.
- [88] A. Pannwitz, O.S. Wenger, *Chem. Commun.* 55 (2019) 4004-4014.
- [89] Y. Liu, Y. Zhao, Y. Sun, J. Cao, H. Wang, X. Wang, H. Huang, M. Shao, Y. Liu, Z. Kang, *Appl. Catal. B* (2020) 118875.
- [90] A. Hwang, A. Bhan, *Acc. Chem. Res.* 52 (2019) 2647-2656.
- [91] T. Ennaert, J. Van Aelst, J. Dijkmans, R. De Clercq, W. Schutyser, M. Dusselier, D. Verboekend, B.F. Sels, *Chem. Soc. Rev.* 45 (2016) 584-611.

- [92] D. Kubička, O. Kikhtyanin, *Catal. Today* 243 (2015) 10-22.
- [93] M. Alvaro, E. Carbonell, B. Ferrer, F.X. Llabrés i Xamena, H. Garcia, *Chem. Eur. J.* 13 (2007) 5106-5112.
- [94] M.D. Allendorf, A. Schwartzberg, V. Stavila, A.A. Talin, *Chem. Eur. J.* 17 (2011) 11372-11388.
- [95] M. Usman, S. Mendiratta, K.L. Lu, *Adv. Mater.* (2016) 1-5.
- [96] Y. Kobayashi, B. Jacobs, M.D. Allendorf, J.R. Long, *Chem. Mater.* 22 (2010) 4120-4122.
- [97] D. Wang, Z. Li, *Res. Chem. Intermed.* 43 (2017) 5169-5186.
- [98] Y. Xu, Y. Chen, W.-F. Fu, *Appl. Catal. B* 236 (2018) 176-183.
- [99] S. Bordiga, C. Lamberti, G. Ricchiardi, L. Regli, F. Bonino, A. Damin, K.-P. Lillerud, M. Bjorgen, A. Zecchina, *Chem. Commun.* (2004) 2300-2301.
- [100] M. Ramyashree, S.S. Priya, N.C. Freudenberg, K. Sudhakar, M. Tahir, *J. CO2 Util.* 43 (2020) 101374.
- [101] M. Karthikeyan, B. Bhagyaraju, C.R. Mariappan, S.M. Mobin, B. Manimaran, *Inorg. Chem. Commun.* 20 (2012) 269-272.
- [102] D. Li, M. Kassymova, X. Cai, S.-Q. Zang, H.-L. Jiang, *Coord. Chem. Rev.* 412 (2020) 213262.
- [103] M. Nemiwal, V. Subbaramaiah, T.C. Zhang, D. Kumar, *Sci. Total Environ.* 762 (2020) 144101.
- [104] M.A. Gordillo, P.A. Benavides, D.K. Panda, S. Saha, *ACS Appl. Mater. Interfaces* 2 (2020) 12955-12961.
- [105] J. Lu, S.-H. Wang, Y. Li, W.-F. Wang, C. Sun, P.-X. Li, F.-K. Zheng, G.-C. Guo, *Dalton Trans.* 49 (2020) 7309-7314.
- [106] M. Karthikeyan, B. Bhagyaraju, C.R. Mariappan, S.M. Mobin, B. Manimaran, *Inorg. Chem. Commun.* 20 (2012) 269-272.
- [107] L. Sun, M.G. Campbell, M. Dincă, *Angew. Chem. Int. Ed.* 55 (2016) 3566-3579.
- [108] J. Calbo, M.J. Golomb, A. Walsh, *J. Mater. Chem. A* 7 (2019) 16571-16597.
- [109] A.J. Clough, J.M. Skelton, C.A. Downes, A.A. De La Rosa, J.W. Yoo, A. Walsh, B.C. Melot, S.C. Marinescu, *J. Am. Chem. Soc.* 139 (2017) 10863-10867.
- [110] C.F. Leong, P.M. Usov, D.M. D'Alessandro, *MRS Bull.* 41 (2016) 858-864.
- [111] L.S. Xie, G. Skorupskii, M. Dincă, *Chem. Rev.* 120 (2020) 8536-8580.
- [112] X. Deng, J.-Y. Hu, J. Luo, W.-M. Liao, J. He, *Top. Curr. Chem.* 378 (2020) 1-50.
- [113] R. Murase, C.F. Leong, D.M. D'Alessandro, *Inorg. Chem.* 56 (2017) 14373-14382.
- [114] M. Usman, S. Mendiratta, S. Batjargal, G. Haider, M. Hayashi, N. Rao Gade, J.-W. Chen, Y.-F. Chen, K.-L. Lu, *ACS Appl. Mater. Interfaces* 7 (2015) 22767-22774.
- [115] D.E. Swanson, J.R. Sites, W.S. Sampath, *Sol. Energy Mater. Sol. Cells* 159 (2017) 389-394.
- [116] S. Jiao, Q. Shen, I.n. Mora-Seró, J. Wang, Z. Pan, K. Zhao, Y. Kuga, X. Zhong, J. Bisquert, *ACS nano* 9 (2015) 908-915.
- [117] P. Sippel, D. Denysenko, A. Loidl, P. Lunkenheimer, G. Sastre, D. Volkmer, *Adv. Funct. Mater.* 24 (2014) 3885-3896.
- [118] T.C. Narayan, T. Miyakai, S. Seki, M. Dincă, *J. Am. Chem. Soc.* 134 (2012) 12932-12935.
- [119] L. Sun, M.G. Campbell, M. Dincă, *Angew. Chem. Int. Ed.* 55 (2016) 3566-3579.
- [120] L. Sun, T. Miyakai, S. Seki, M. Dincă, *J. Am. Chem. Soc.* 135 (2013) 8185-8188.
- [121] D. Sheberla, L. Sun, M.A. Blood-Forsythe, S.I. Er, C.R. Wade, C.K. Brozek, A.n. Aspuru-Guzik, M. Dincă, *J. Am. Chem. Soc.* 136 (2014) 8859-8862.
- [122] S. Sen, T. Yamada, H. Kitagawa, P.K. Bharadwaj, *Cryst. Growth Des.* 14 (2014) 1240-1244.
- [123] H. Ōkawa, M. Sadakiyo, T. Yamada, M. Maesato, M. Ohba, H. Kitagawa, *J. Am. Chem. Soc.* 135 (2013) 2256-2262.
- [124] G.K. Shimizu, J.M. Taylor, S. Kim, *Science* 341 (2013) 354-355.
- [125] O.M. Yaghi, M. O'keeffe, N.W. Ockwig, H.K. Chae, M. Eddaoudi, J. Kim, *Nature* 423 (2003) 705.
- [126] I. Stassen, N. Burtch, A. Talin, P. Falcaro, M. Allendorf, R. Ameloot, *Chem. Soc. Rev.* 46 (2017) 3185-3241.
- [127] E.A. Dolgoplova, A.J. Brandt, O.A. Ejegbavwo, A.S. Duke, T.D. Maddumapatabandi, R.P. Galhenage, B.W. Larson, O.G. Reid, S.C. Ammal, A. Heyden, *J. Am. Chem. Soc.* 139 (2017) 5201-5209.

- [128] X. Huang, Y. Li, Y. Chen, H. Zhou, X. Duan, Y. Huang, *Angew. Chem. Int. Ed.* 52 (2013) 6063-6067.
- [129] W. Jiang, Q. Ruan, J. Xie, X. Chen, Y. Zhu, J. Tang, *Appl. Catal. B* 236 (2018) 428-435.
- [130] M. Xiao, B. Luo, S. Wang, L. Wang, J. *Energy Chem.* 27 (2018) 1111-1123.
- [131] K.L. Skubi, T.R. Blum, T.P. Yoon, *Chem. Rev.* 116 (2016) 10035-10074.
- [132] X. Deng, Z. Li, H. García, *Chem. Eur. J.* 23 (2017) 11189-11209.
- [133] Y. Yang, X. Liu, Z. Guo, H. Zhan, *Inorg. Chem. Commun.* 92 (2018) 18-21.
- [134] T. Toyao, M. Saito, S. Dohshi, K. Mochizuki, M. Iwata, H. Higashimura, Y. Horiuchi, M. Matsuoka, *Chem. Commun.* 50 (2014) 6779-6781.
- [135] R. Yan, Y. Zhao, H. Yang, X.J. Kang, C. Wang, L.L. Wen, Z.D. Lu, *Adv. Funct. Mater.* 28 (2018) 1802021.
- [136] C. Xu, H. Liu, D. Li, J.-H. Su, H.-L. Jiang, *Chem. Sci.* 9 (2018) 3152-3158.
- [137] M. Gutierrez, B. Cohen, F. Sánchez, A. Douhal, *Phys. Chem. Chem. Phys.* 18 (2016) 27761-27774.
- [138] K.G. Laurier, F. Vermoortele, R. Ameloot, D.E. De Vos, J. Hofkens, M.B. Roeffaers, J. *Am. Chem. Soc.* 135 (2013) 14488-14491.
- [139] E.M. Dias, C. Petit, J. Mater. Chem. A 3 (2015) 22484-22506.
- [140] C. Gomes Silva, I. Luz, F.X. Llabrés i Xamena, A. Corma, H. García, *Chem. Eur. J.* 16 (2010) 11133-11138.
- [141] M. Wang, D. Wang, Z. Li, *Appl. Catal. B* 183 (2016) 47-52.
- [142] D. Wang, M. Wang, Z. Li, *ACS Catal.* 5 (2015) 6852-6857.
- [143] Y. Ma, Z. Wang, X. Xu, J. Wang, *Chin. J. Catal.* 38 (2017) 1956-1969.
- [144] A. Dhakshinamoorthy, A.M. Asiri, H. Garcia, *Angew. Chem. Int. Ed.* 55 (2016) 5414-5445.
- [145] Y. Yamakoshi, N. Umezawa, A. Ryu, K. Arakane, N. Miyata, Y. Goda, T. Masumizu, T. Nagano, *J. Am. Chem. Soc.* 125 (2003) 12803-12809.
- [146] Q. Liu, Y.N. Li, H.H. Zhang, B. Chen, C.H. Tung, L.Z. Wu, *Chem. Eur. J.* 18 (2012) 620-627.
- [147] E. Karamian, S. Sharifnia, *J. CO2 Util.* 16 (2016) 194-203.
- [148] S. Kreft, D. Wei, H. Junge, M. Beller, *EnergyChem* 2 (2020) 100044.
- [149] L. Liu, Y. Li, *Aerosol Air Qual. Res.* 14 (2014) 453-469.
- [150] R.R. Ikreedeegh, M. Tahir, *J. CO2 Util.* 43 (2021) 101381.
- [151] N. Shehzad, M. Tahir, K. Johari, T. Murugesan, M. Hussain, *J. CO2 Util.* 26 (2018) 98-122.
- [152] J. Fu, K. Jiang, X. Qiu, J. Yu, M. Liu, *Mater. Today* 32 (2020) 222-243.
- [153] M. Wang, D. Wang, Z. Li, *Appl. Catal. B.* 183 (2016) 47-52.
- [154] X.-K. Wang, J. Liu, L. Zhang, L.-Z. Dong, S.-L. Li, Y.-H. Kan, D.-S. Li, Y.-Q. Lan, *ACS Catal.* 9 (2019) 1726-1732.
- [155] Q. Huang, J. Liu, L. Feng, Q. Wang, W. Guan, L.-Z. Dong, L. Zhang, L.-K. Yan, Y.-Q. Lan, H.-C. Zhou, *Natl. Sci. Rev.* 7 (2020) 53-63.
- [156] J. Becerra, D.-T. Nguyen, V.-N. Gopalakrishnan, T.-O. Do, *ACS Appl. Energy Mater.* 3 (2020) 7659-7665.
- [157] K. Niu, Y. Xu, H. Wang, R. Ye, H.L. Xin, F. Lin, C. Tian, Y. Lum, K.C. Bustillo, M.M. Doeff, *Science Adv.* 3 (2017) e1700921.
- [158] S. Chen, G. Hai, H. Gao, X. Chen, A. Li, X. Zhang, W. Dong, *Chem. Eng. J.* 406 (2021) 126886.
- [159] A. Kidanemariam, J. Lee, J. Park, *Polymer* 11 (2019) 2090.
- [160] E.A. Dolgoplova, A.M. Rice, C.R. Martin, N.B. Shustova, *Chem. Soc. Rev.* 47 (2018) 4710-4728.
- [161] G. Maurin, C. Serre, A. Cooper, G. Férey, *Chem. Soc. Rev.* 46 (2017) 3104-3107.
- [162] Z. Yin, S. Wan, J. Yang, M. Kurmoo, M.-H. Zeng, *Coord. Chem. Rev.* 378 (2019) 500-512.
- [163] P. Zhao, R. Li, W. Wu, J. Wang, J. Liu, Y. Zhang, *Compos. B. Eng.* 176 (2019) 107208.
- [164] J. Qiu, X. Zhang, Y. Feng, X. Zhang, H. Wang, J. Yao, *Appl. Catal. B* 231 (2018) 317-342.
- [165] M.B. Majewski, A.W. Peters, M.R. Wasielewski, J.T. Hupp, O.K. Farha, *ACS Energy Lett.* 3 (2018) 598-611.
- [166] M. Sun, S. Yan, Y. Sun, X. Yang, Z. Guo, J. Du, D. Chen, P. Chen, H. Xing, *Dalton Trans.* 47 (2018) 909-915.
- [167] D. Chen, H. Xing, C. Wang, Z. Su, *J. Mater. Chem. A* 4 (2016) 2657-2662.

- [168] H.-Q. Xu, J. Hu, D. Wang, Z. Li, Q. Zhang, Y. Luo, S.-H. Yu, H.-L. Jiang, *J. Am. Chem. Soc.* 137 (2015) 13440-13443.
- [169] H. Vardhan, A. Mehta, C.I. Ezugwu, F. Verpoort, *Polyhedron* 112 (2016) 104-108.
- [170] P. Wu, X. Guo, L. Cheng, C. He, J. Wang, C. Duan, *Inorg. Chem.* 55 (2016) 8153-8159.
- [171] C.H. Hendon, D. Tiana, M. Fontecave, C.m. Sanchez, L. D'arras, C. Sassoeye, L. Rozes, C. Mellot-Draznieks, A. Walsh, *J. Am. Chem. Soc.* 135 (2013) 10942-10945.
- [172] Y. Lee, S. Kim, J.K. Kang, S.M. Cohen, *Chem. Commun.* 51 (2015) 5735-5738.
- [173] J. Gascon, M.D. Hernández-Alonso, A.R. Almeida, G.P. van Klink, F. Kapteijn, G. Mul, *ChemSusChem* 1 (2008) 981-983.
- [174] M.W. Logan, S. Ayad, J.D. Adamson, T. Dilbeck, K. Hanson, F.J. Uribe-Romo, *J. Mater. Chem. A* 5 (2017) 11854-11863.
- [175] J.L. White, M.F. Baruch, J.E. Pander III, Y. Hu, I.C. Fortmeyer, J.E. Park, T. Zhang, K. Liao, J. Gu, Y. Yan, *Chem. Rev.* 115 (2015) 12888-12935.
- [176] K. Maeda, *Adv. Mater.* 31 (2019) 1808205.
- [177] A. Nakada, R. Kuriki, K. Sekizawa, S. Nishioka, J.J.M. Vequizo, T. Uchiyama, N. Kawakami, D. Lu, A. Yamakata, Y. Uchimoto, *ACS Catal.* 8 (2018) 9744-9754.
- [178] C.S. Diercks, Y. Liu, K.E. Cordova, O.M. Yaghi, *Nat. Mater.* (2018) 1.
- [179] J. Lee, O.K. Farha, J. Roberts, K.A. Scheidt, S.T. Nguyen, J.T. Hupp, *Chem. Soc. Rev.* 38 (2009) 1450-1459.
- [180] M. Nasalevich, M. Van der Veen, F. Kapteijn, J. Gascon, *CrystEngComm* 16 (2014) 4919-4926.
- [181] C. Wang, Z. Xie, W. Lin, *J. Am. Chem. Soc.* 133 (2011) 13445-13454.
- [182] H.S. Lee, S. Jee, R. Kim, H.-T. Bui, B. Kim, J.-K. Kim, K.S. Park, W. Choi, W. Kim, K.M. Choi, *Energy Environ. Sci.* 13 (2020) 519-526.
- [183] R. Huang, Y. Peng, C. Wang, Z. Shi, W. Lin, *Eur. J. Inorg. Chem.* 2016 (2016) 4358-4362.
- [184] H. Fei, M.D. Sampson, Y. Lee, C.P. Kubiak, S.M. Cohen, *Inorg. Chem.* 54 (2015) 6821-6828.
- [185] M.B. Chambers, X. Wang, N. Elgrishi, C.H. Hendon, A. Walsh, J. Bonnefoy, J. Canivet, E.A. Quadrelli, D. Farrusseng, C. Mellot-Draznieks, *ChemSusChem* 8 (2015) 603-608.
- [186] X. Wang, F.M. Wisser, J. Canivet, M. Fontecave, C. Mellot-Draznieks, *ChemSusChem* 11 (2018) 3315-3322.
- [187] Y. Liu, Y. Yang, Q. Sun, Z. Wang, B. Huang, Y. Dai, X. Qin, X. Zhang, *ACS Appl. Mater. Interfaces* 5 (2013) 7654-7658.
- [188] J. Zhao, Q. Wang, C. Sun, T. Zheng, L. Yan, M. Li, K. Shao, X. Wang, Z. Su, *J. Mater. Chem. A* 5 (2017) 12498-12505.
- [189] S. Zhang, L. Li, S. Zhao, Z. Sun, J. Luo, *Inorg. Chem.* 54 (2015) 8375-8379.
- [190] D.C. Liu, T. Ouyang, R. Xiao, W.J. Liu, D.C. Zhong, Z. Xu, T.B. Lu, *ChemSusChem* 12 (2019) 2166-2170.
- [191] U.J. Ryu, S.J. Kim, H.-K. Lim, H. Kim, K.M. Choi, J.K. Kang, *Sci. Rep.* 7 (2017) 612.
- [192] D. Sun, Y. Gao, J. Fu, X. Zeng, Z. Chen, Z. Li, *Chem. Commun.* 51 (2015) 2645-2648.
- [193] H. Rao, J. Bonin, M. Robert, *ChemSusChem* 10 (2017) 4447-4450.
- [194] Z. Guo, S. Cheng, C. Cometto, E. Anxolabéhère-Mallart, S.-M. Ng, C.-C. Ko, G. Liu, L. Chen, M. Robert, T.-C. Lau, *J. Am. Chem. Soc.* 138 (2016) 9413-9416.
- [195] J.-X. Zhang, C.-Y. Hu, W. Wang, H. Wang, Z.-Y. Bian, *Appl. Catal. A* 522 (2016) 145-151.
- [196] A. Call, M. Cibian, K. Yamamoto, T. Nakazono, K. Yamauchi, K. Sakai, *ACS Catal.* 9 (2019) 4867-4874.
- [197] A. Fateeva, S. Devautour-Vinot, N. Heymans, T. Devic, J.-M. Greneche, S. Wuttke, S. Miller, A. Lago, C. Serre, G. De Weireld, *Chem. Mater.* 23 (2011) 4641-4651.
- [198] C.Y. Lee, O.K. Farha, B.J. Hong, A.A. Sarjeant, S.T. Nguyen, J.T. Hupp, *J. Am. Chem. Soc.* 133 (2011) 15858-15861.
- [199] A. Fateeva, P.A. Chater, C.P. Ireland, A.A. Tahir, Y.Z. Khimyak, P.V. Wiper, J.R. Darwent, M.J. Rosseinsky, *Angew. Chem. Int. Ed.* 51 (2012) 7440-7444.
- [200] A. Aziz, A.R. Ruiz-Salvador, N.C. Hernández, S. Calero, S. Hamad, R. Grau-Crespo, *J. Mater. Chem. A* 5 (2017) 11894-11904.
- [201] Y. Li, Q. Duan, H. Wang, B. Gao, N. Qiu, Y. Li, *J. Photochem. Photobiol. A* 356 (2018) 370-378.
- [202] X. Wang, X. Zhang, W. Zhou, L. Liu, J. Ye, D. Wang, *Nano Energy* 62 (2019) 250-258.

- [203] E.X. Chen, M. Qiu, Y.F. Zhang, Y.S. Zhu, L.Y. Liu, Y.Y. Sun, X. Bu, J. Zhang, Q. Lin, *Adv. Mater.* 30 (2018) 1704388.
- [204] Z.-H. Yan, M.-H. Du, J. Liu, S. Jin, C. Wang, G.-L. Zhuang, X.-J. Kong, L.-S. Long, L.-S. Zheng, *Nat. Commun.* 9 (2018) 1-9.
- [205] Z.-B. Fang, T.-T. Liu, J. Liu, S. Jin, X.-P. Wu, X.-Q. Gong, K. Wang, Q. Yin, T.-F. Liu, R. Cao, *J. Am. Chem. Soc.* 142 (2020) 12515-12523.
- [206] M. Dan-Hardi, C. Serre, T. Frot, L. Rozes, G. Maurin, C. Sanchez, G. Férey, *J. Am. Chem. Soc.* 131 (2009) 10857-10859.
- [207] M. de Miguel, F. Ragon, T. Devic, C. Serre, P. Horcajada, H. García, *ChemPhysChem* 13 (2012) 3651-3654.
- [208] D. Sun, W. Liu, M. Qiu, Y. Zhang, Z. Li, *Chem. Commun.* 51 (2015) 2056-2059.
- [209] S. Wang, W. Yao, J. Lin, Z. Ding, X. Wang, *Angew. Chem. Int. Ed.* 53 (2014) 1034-1038.
- [210] S. Wang, X. Wang, *Appl. Catal. B* 162 (2015) 494-500.
- [211] D. Sun, W. Liu, Y. Fu, Z. Fang, F. Sun, X. Fu, Y. Zhang, Z. Li, *Chem. Eur. J.* 20 (2014) 4780-4788.
- [212] M. Siegert, J.M. Sonawane, C.I. Ezugwu, R. Prasad, Economic assessment of nanomaterials in bio-electrical water treatment, in: Prasad R., Karchiyappan T. (eds), *Advanced Research in Nanosciences for Water Technology, Nanotechnology in the Life Sciences*, Springer 2019, pp. 1-23.
- [213] N. Li, J. Liu, J.J. Liu, L.Z. Dong, Z.F. Xin, Y.L. Teng, Y.Q. Lan, *Angew. Chem.* 131 (2019) 5280-5285.
- [214] J. Liu, Y.-Z. Fan, X. Li, Z. Wei, Y.-W. Xu, L. Zhang, C.-Y. Su, *Appl. Catal. B* 231 (2018) 173-181.
- [215] A. Upadhyaya, G. Rincón, J. Water Resour. Prot. 11 (2019) 1207.
- [216] C. Liu, D. Mao, J. Pan, J. Qian, W. Zhang, F. Chen, Z. Chen, Y. Song, *J. Rare Earths* 37 (2019) 1269-1278.
- [217] R. Li, J. Hu, M. Deng, H. Wang, X. Wang, Y. Hu, H.L. Jiang, J. Jiang, Q. Zhang, Y. Xie, *Adv. Mater.* 26 (2014) 4783-4788.
- [218] K.M. Choi, D. Kim, B. Rungtaweevoranit, C.A. Trickett, J.T.D. Barmanbek, A.S. Alshammari, P. Yang, O.M. Yaghi, *J. Am. Chem. Soc.* 139 (2016) 356-362.
- [219] K. Khaletskaya, A. Pougin, R. Medishetty, C. Rösler, C. Wiktor, J. Strunk, R.A. Fischer, *Chem. Mater.* 27 (2015) 7248-7257.
- [220] H. Zhang, J. Wei, J. Dong, G. Liu, L. Shi, P. An, G. Zhao, J. Kong, X. Wang, X. Meng, *Angew. Chem.* 128 (2016) 14522-14526.
- [221] Y. Su, Z. Zhang, H. Liu, Y. Wang, *Appl. Catal. B* 200 (2017) 448-457.
- [222] H. Zhao, X. Wang, J.-F. Feng, Y. Chen, X. Yang, S. Gao, R. Cao, *Catal. Sci. Technol.* 8 (2018) 1288-1295.
- [223] L. Shi, T. Wang, H. Zhang, K. Chang, J. Ye, *Adv. Funct. Mater.* 25 (2015) 5360-5367.
- [224] F. Yu, L. Chen, X. Shen, X. Li, C. Duan, *APL Mater.* 7 (2019) 101101.
- [225] J.W. Maina, J.r.A. Schütz, L. Grundy, E. Des Ligneris, Z. Yi, L. Kong, C. Pozo-Gonzalo, M. Ionescu, L.F. Dumée, *ACS Appl. Mater. Interfaces* 9 (2017) 35010-35017.
- [226] Y. Xu, J. Mo, G. Xie, D. Ding, S. Ding, X. Wang, C. Li, *Chem. Commun.* 55 (2019) 6862-6865.
- [227] D. Ding, Z. Jiang, J. Jin, J. Li, D. Ji, Y. Zhang, L. Zan, *J. Catal.* 375 (2019) 21-31.
- [228] X. Jing, C. He, Y. Yang, C. Duan, *J. Am. Chem. Soc.* 137 (2015) 3967-3974.
- [229] L.Y. Wu, Y.F. Mu, X.X. Guo, W. Zhang, Z.M. Zhang, M. Zhang, T.B. Lu, *Angew. Chem. Int. Ed.* 58 (2019) 9491-9495.
- [230] S. Wang, J. Lin, X. Wang, *Phys. Chem. Chem. Phys.* 16 (2014) 14656-14660.
- [231] Q. Liu, Z.-X. Low, L. Li, A. Razmjou, K. Wang, J. Yao, H. Wang, *J. Mater. Chem. A* 1 (2013) 11563-11569.
- [232] L. Ye, Y. Gao, S. Cao, H. Chen, Y. Yao, J. Hou, L. Sun, *Appl. Catal. B* 227 (2018) 54-60.
- [233] N. Sadeghi, S. Sharifnia, T.-O. Do, *J. Mater. Chem. A* 6 (2018) 18031-18035.
- [234] Y. Gao, L. Zhang, Y. Gu, W. Zhang, Y. Pan, W. Fang, J. Ma, Y.-Q. Lan, J. Bai, *Chem. Sci.* 11 (2020) 10143-10148.
- [235] L.-W. Lee, Y.-C. Kao, M.-Y. Chung, B.-C. Chang, G.-H. Lee, S.-M. Peng, C.-M. Wang, Y.-H. Liu, S.-L. Lee, K.-L. Lu, *Dalton Trans.* 48 (2019) 1950-1954.
- [236] Y. Kim, S. Das, S. Bhattacharya, S. Hong, M.G. Kim, M. Yoon, S. Natarajan, K. Kim, *Chem. Eur. J.* 18 (2012) 16642-16648.
- [237] K. Asha, R. Bhattacharjee, S. Mandal, *Angew. Chem. Int. Ed.* 55 (2016) 11528-11532.

- [238] R. Zou, P.Z. Li, Y.F. Zeng, J. Liu, R. Zhao, H. Duan, Z. Luo, J.G. Wang, R. Zou, Y. Zhao, *Small* 12 (2016) 2334-2343.
- [239] W. Lin, H. Frei, *J. Am. Chem. Soc.* 127 (2005) 1610-1611.
- [240] T.-H. Xie, X. Sun, J. Lin, *J. Phys. Chem. C* 112 (2008) 9753-9759.
- [241] H. Han, H. Frei, *J. Phys. Chem. C* 112 (2008) 8391-8399.
- [242] C.K. Brozek, M. Dincă, *J. Am. Chem. Soc.* 135 (2013) 12886-12891.
- [243] S. Das, H. Kim, K. Kim, *J. Am. Chem. Soc.* 131 (2009) 3814-3815.
- [244] M. Kim, J.F. Cahill, H. Fei, K.A. Prather, S.M. Cohen, *J. Am. Chem. Soc.* 134 (2012) 18082-18088.
- [245] A. Torrisi, C. Mellot-Draznieks, R.G. Bell, *J. Chem. Phys* 132 (2010) 044705.
- [246] A. Torrisi, R.G. Bell, C. Mellot-Draznieks, *Cryst. Growth Des.* 10 (2010) 2839-2841.
- [247] I.A. Ibarra, A. Mace, S. Yang, J. Sun, S. Lee, J.-S. Chang, A. Laaksonen, M. Schröder, X. Zou, *Inorg. Chem.* 55 (2016) 7219-7228.
- [248] R.W. Stevens Jr, R.V. Siriwardane, J. Logan, *Energy Fuels* 22 (2008) 3070-3079.
- [249] P. Valvekens, F. Vermoortele, D. De Vos, *Catal. Sci. Technol.* 3 (2013) 1435-1445.
- [250] C.H. Lau, R. Babarao, M.R. Hill, *Chem. Commun.* 49 (2013) 3634-3636.
- [251] J.-M. Yang, Z.-P. Qi, Y.-S. Kang, Q. Liu, W.-Y. Sun, *Chin. Chem. Lett.* 27 (2016) 492-496.
- [252] S. Zhang, L. Li, S. Zhao, Z. Sun, M. Hong, J. Luo, *J. Mater. Chem. A* 3 (2015) 15764-15768.
- [253] M. Wang, J. Liu, C. Guo, X. Gao, C. Gong, Y. Wang, B. Liu, X. Li, G.G. Gurzadyan, *J. Mater. Chem. A* 6 (2018) 4768-4775.
- [254] X.-Y. Dao, J.-H. Guo, X.-Y. Zhang, S.-Q. Wang, X.-M. Cheng, W.-Y. Sun, *J. Mater. Chem. A* 8 (2020) 25850-25856.